Title
Comparison of Community Climate System Model Simulations and Paleoclimate Data for the Western Pacific Warm Pool Climate during the Last Glacial Maximum

Author
Pittman, Dustin

Publication Date
2012

Peer reviewed|Thesis/dissertation

University of California

Los Angeles

Comparison of Community Climate System Model Simulations and Paleoclimate Data for the Western Pacific Warm Pool Climate during the Last Glacial Maximum

A thesis submitted in partial satisfaction

of the requirements for the degree

Master of Science in Atmospheric and Oceanic Sciences

by

Dustin Edwin Pittman

2012

Abstract of the Thesis

Comparison of Community Climate System Model Simulations and Paleoclimate Data for the Western Pacific Warm Pool Climate during the Last Glacial Maximum

by

Dustin Edwin Pittman

Master of Science in Atmospheric and Oceanic Sciences

University of California, Los Angeles, 2012

Professor Aradhna Tripati, Chair

A highly debated research topic has been understanding the magnitude of tropical cooling in the western Pacific warm pool (WPWP) from the Last Glacial Maximum (LGM) to present-day. Paleoclimate data indicates a range of LGM cooling from 1-5°C. Using a radiative-convective model with an entraining plume calculation, the present-day and LGM snowlines can be explained with a ∼3.5°C surface cooling in the WPWP during the LGM. NCAR's CCSM 3 and 4 simulate LGM cooling of ∼2°C. By comparing the results of CCSM3 and CCSM4, the higher resolution CCSM4 replicated LGM boundary conditions more accurately, increased LGM precipitation rates ∼0.4 mm/day, and reduced the transport of drier subtropical air from the Northern Hemisphere into the WPWP. One of the major issues in the CCSM identified in this thesis is the propagation of a temperature signal associated with the boundary layer over mountains to the upper-levels of the troposphere.

The thesis of Dustin Edwin Pittman is approved.

David Neelin

Jonathan Mitchell

Aradhna Tripati, Committee Chair

University of California, Los Angeles

2012

Table of Contents

List of Figures

List of Tables

CHAPTER 1

Introduction

The focus of this paper is to investigate the cause of LGM to present-day land and ocean-based warming in the WPWP as well as changes in the lower tropospheric structure. Emphasis is placed on how the two most recent CCSM versions of general circulation models (GCMs) reproduce LGM conditions at the surface and in the structure of the vertical temperature compared to paleoclimate proxy data. This analysis will demonstrate each models regional climate accuracies, show biases, determine enhancement of updated model versions, and give insight of climate conditions of the WPWP during the LGM. The latter point will assist with understanding mass transport, regions of enhanced precipitation/evaporation, and piece together a more thorough representation of the WPWP's moisture transport to higher latitudes.

In order to accomplish the objectives listed above, an analysis of present-day vertical temperature profiles, sea and land surface temperatures, and tropical mountain snowlines was conducted. From this analysis, a reconstruction of average present-day vertical temperatures in comparison to the snowline dataset is created to determine the surface temperature and relative humidity at the surface and the free troposphere, in addition, to the atmospheric freezing level deviations from the moist adiabat and observations, respectively. The third ob-

jective, carried out collaboratively as discussed in the text, is to model the effects of changing surface temperature, surface and free tropospheric relative humidity, and the magnitude of parameterized entrainment on the height of the atmospheric freezing level and WPWP lapse rate during the LGM. The fourth objective is to compare CCSM3 and CCSM4 variable changes from LGM to the pre-industrial era, informed by the results of the previous objectives. This analysis is followed by an exploration of effects an updated entrainment scheme in CCSM4 compared to CCSM3 has on model variables. Changes in the large-scale mass transport during the LGM are the final objective followed by any other possible causes for the climate of the WPWP during the LGM.

1.1 Last Glacial Maximum

The Last Glacial Maximum (LGM) is the most recent time in Earth's history when ice covered large portions of North America and northern Eurasia and occurred approximately 21,000 calendar years BP [42, 43, 44]. Expanded continental ice and reduced atmospheric CO_2 levels are found to have had a substantial impact on the global mean temperature [6, 33] and more locally on atmospheric and oceanic temperatures. The circulation of the atmosphere and oceans was also substantially different from present. For example, the Laurentide ice sheet covered large portions of North America helping to reduce the global sea level by $\sim$120 meters (m) [31], increasing the topography of North America and changing patterns of circulation around the continent [41]. In addition there was an equatorward displacement of cooler temperatures along with subtropical highs (the latter being more pronounced in the Northern Hemisphere) [41].

Thus the LGM provides climate scientists a time interval with well-constrained boundary conditions that can be used to test the accuracy of GCMs in simulating atmospheric and oceanic conditions different from today. Ice cores hold information on the atmospheric composition during this time period which provides scientists with historic levels of important LGM greenhouse gas concentrations: CO_2 = 185 ppm, CH_4 = 350 ppb and N_2O = 200 ppb [12, 17, 37]. These values are generally agreed upon throughout the scientific community, however land and ocean surface temperatures during the LGM are less certain. There have been many research projects aimed at addressing how much land and ocean temperatures have changed since the LGM. The first major research project to undertake producing a compilation of data for the LGM in a systematic fashion was the CLIMAP (Climate: Long range Investigation, Mapping, and Prediction) group in the 1970s and 1980s. The goal of this research endeavor was to take quantitative geologic evidence to reconstruct boundary conditions for the climate at the LGM [8].

Figure 5.1 shows a reconstructed sea surface temperature map from CLIMAP's first research compilation. In order to reconstruct sea surface temperatures (SSTs) 18,000 BP, the CLIMAP Project Members used biological transfer functions, which determine past surface temperatures by the translation of numerical descriptions of the planktonic biota preserved in deep-sea sediments into estimates of past seasonal SSTs [8]. The *CLIMAP Project Members* (1976) found three key boundary conditions for the LGM: (1) there was a large increase in the surface albedo as glacial and desert expansion occurred, (2) the world surface ocean temperature change was not as large as initially thought, with an average global reduction of 2.3°C, and (3) there was increased upwelling along the coasts

of continents. However, the cooler upwelled waters from the eastern Pacific Ocean did not reach the western Pacific Ocean where glacial surface ocean temperatures were little different from present-day.

The CLIMAP reconstructions were the first of its kind, however as more research has been done, some of the methods that were used have come under investigation. A large controversy with the CLIMAP project was the reconstructed $\sim$1°C mean decrease in tropical SSTs as this value is not consistent with lowered tropical snow lines as well as evidence from various δ^{18}O proxies showing the tropics were 4-6°C cooler than present-day [63]. The topic of lowering tropical snow lines and the effect this had on the tropical lapse rates will be discussed later in this thesis.

A more recent attempt to synthesize reconstructions of surface temperatures in order to produce a map of global SSTs during the LGM was done by the MARGO (Multiproxy Approach for the Reconstruction of the Glacial Ocean surface) working group. The MARGO project initiated in September 2002 with a main objective of collating all the available proxy data and transfer function techniques, and placing them into a common framework for a multi-proxy global glacial ocean reconstruction [30]. MARGO differs from CLIMAP as it relies on a multitude of proxy methods to reconstruct temperatures and therefore should hypothetically be an all-encompassing representation of the LGM global climate. Additionally, the accuracy and understanding of radiocarbon dating has increased significantly since CLIMAP resulting in a more encompassing LGM period in the MARGO dataset (16,000-26,000 years BP for the CLIMAP versus 19,000-23,000 years BP for MARGO).

The MARGO working group's largest task involved compiling a new dataset

for oxygen isotope data from different paleoclimate proxy records. An emphasis was placed on oxygen isotopes as they provide a first approximation of the surface density of the ocean since the oxygen isotopic composition of planktonic foraminifera is a function of salinity and temperature [30]. The compiled dataset (Figure 5.2) consists of over 2,100 recent sediment measurements and 410 data points from LGM sediments with an age control applied.

There exist several challenges to the MARGO project compilation of a unique multi-proxy SST, sea surface salinity, and sea-ice dataset. The dataset has a level of disagreement between proxies, which was expected because each approach has differing assumptions involved in interpretation, and because each proxy is sensitive to different processes [30]. Each proxy rarely reflects simply one climatic parameter; all proxy reconstructions provide slightly or substantially different SST estimates. In addition, the meaning of whether the proxy reflects sea surface conditions and/or temperature is still a matter of debate, as is the season it reflects. Meaning the surface temperature could be derived from a species that was predominately located several meters below sea surface, but since humans were not around during this time period there is no exact way to infer this information.

The synthesis from the MARGO project is composed of 696 individual SST reconstructions with dense coverage in the northern Atlantic Ocean, Southern Ocean, and the Tropics, but with poor coverage in subtropical ocean gyres. The SST anomalies were constructed using the World Ocean Atlas SSTs (LGMWOA SST) showing an overall agreement in magnitude of latitudinal anomalies between geochemical and microfossil proxies [34]. The proxy temperatures were most robust in the region from 30°S-30°N as seen in Figure 5.3. The MARGO tropical

cooling is more extensive than proposed by CLIMAP with a 1-3°C cooling of the WPWP supported by three proxy records [34]. Overall the tropical Pacific band (15°S-15°N) experienced an LGM cooling of 1.2±1.1°C.

1.2 Western Tropical Pacific Warm Pool

The tropical Pacific Ocean is the area located between the latitudinal band from 23°N-23°S extending from South America to the Maritime Continent. The western portion is characterized by high SSTs and large amounts of precipitation. It lies within the bounds of the rising branches of the Hadley Cell and Walker Circulation and therefore the Inter-tropical Convergence Zone (ITCZ).

The tropical Pacific Ocean is a significant heat transfer region between the atmosphere and the ocean. The WPWP plays a key role in the strength of the Walker Circulation and consequently has a significant influence on El Nino Southern Oscillation (ENSO) phenomena [13]. The impacts from changes in the SST of the central and eastern regions of the Pacific Ocean have corresponding global effects as evident from global ENSO impacts. Such impacts range from droughts in the Maritime Continent to flooding in the southwest United States. In addition to causing extreme weather events, the Pacific Ocean is a principle transporter of moisture and heat from the tropics toward the Polar Regions and a vital source of water vapor into the troposphere [48]. The majority of this transport occurs in the WPWP, which is the focus region for this paper.

The WPWP is a region in the western-most part of the tropical Pacific Ocean with SSTs typically larger than 28°C. It is generally understood that SSTs in this region are ∼1°C larger than the atmospheric air just above the surface called

the skin temperature [13]. For the analysis presented in this thesis, the extent of the WPWP is defined as 15°N-15°S and 135°W-165°W. The high SSTs of the WPWP initiate large amounts of atmospheric convection thus transporting large amounts of surface and boundary layer moisture and heat to the upper parts of the troposphere. This process is important as most of this vertically transported heat and moisture fans out horizontally as it reaches the middle and upper levels of the troposphere. The large amount of horizontal transport coming from the WPWP is one of the principal mechanisms for moving heat and moisture out of the tropics.

The movement of moisture and heat out of the tropics acts to balance the temperature and moisture gradients between the tropics and the Polar Regions. Without this large quantity of heat and moisture transport, regions outside the tropics would be colder with less available moisture leading to drier climates. Therefore the WPWP SSTs and the amount of atmospheric convection are pivotal factors in influencing climates elsewhere around the globe, as well as global climate.

This thesis will discuss changes in WPWP climate during the Last Glacial Maximum by comparing GCM simulations to paleoclimate proxy records.

1.3 Proxy data and Snow Line data

Paleoclimate data is an important aspect of this research as it provides past temperature estimates for specific regions, both land and ocean. Proxy data can be compared with model results in an effort to determine if models are accurately reconstructing past climates and examine which aspects of the model need ad-

justed (e.g., SSTs, land surface temperatures, precipitation). The reconstructed temperatures not only play a role in surface processes, but also can be used to constrain lapse rates and enhance our understanding of the vertical atmospheric temperature structure during the LGM by combining surface values from the ocean or land with upper-level data from glacial extent (snow lines) or other proxies.

Most studies, including MARGO, find evidence for a 1°C surface cooling in the WPWP [9, 34], but the uncertainties associated with this estimate are as large as 2°C. However recent studies utilizing new proxies indicate the WPWP was much cooler at the LGM, by as much as 3-5°C [61]. Foraminiferal Mg/Ca ratios show mean temperatures in the WPWP cooled by 2.5°C±0.7°C during the LGM [13, 32, 34]. The surface foraminifera used in *de Garidel-Thoron et al.* (2007) was *Globigerinoides ruber* (G. ruber) from the ocean sediment core MD97-2138 (1°25'S, 146°24'E, 1900m deep) and the Mg/Ca measurements were done following the analytical protocol detailed by *Rosenthal et al.* (1999). The outcomes from this study are robust with Mg/Ca results from nearby cores in the WPWP [13]. Several uncertainties with the Mg/Ca paleothermometry technique include one or a combination of the following as discussed in the paper by *de Garidel-Thoron et al.* (2007): variable dissolution effects on each record, mixing of glacial and interglacial sediments in low sedimentation rate cores, and methodological differences among laboratories. One problem with Mg/Ca-based temperature proxy estimates and other paleothermometry records is most come from different sediment cores resulting in the possibility for differing results on the regional scale.

Another study examined how salinity changes during the LGM effected tem-

peratures and consequently reported a salinity-corrected Mg/Ca temperature change of ∼4°C [35]. The sea surface salinity (SSS) effect on the Mg/Ca ratio is important as the ocean salinity increased to values ∼1.15 psu higher [1] than present-day during the LGM due to freshwater being locked up on the continents and ocean volume decreased as continental glaciers expanded. According to *Mathien-Blard and Bassinot* (2009), Mg/Ca-based SST could be biased by ∼1.6°C if the effects of changing salinity was not taken into account. However, the salinity-correct Mg/Ca method has two uncertainties that lead to difficulties in precisely determining the LGM SSTs: constraining the global SSS-$\delta^{18}O_{sw}$ relationship which is induced by waxing/waning of the continental ice sheets and knowing the past regional SSS-$\delta^{18}O_{sw}$ relationship which is controlled by evaporation and precipitation mechanisms and continental runoff.

Reconstructions in the South Pacific show an even larger temperature change via coral data of Sr/Ca of ∼5°C near Vanuatu in the southwestern Pacific Ocean (15°S, 167°E) [3] which are consistent with estimates of tropical temperatures from corals in the Atlantic Ocean [20]. From the paper *Beck et al.* (1992), the ratio of incorporation of Strontium to Calcium in corals is controlled by two factors: the Sr/Ca activity ratio of the ocean and the Sr/Ca distribution coefficient between aragonite and seawater. The latter depends on the temperature of the seawater in which the coral grew but is only a weak function of the chemical composition of water [3]. One factor used in determining past SSTs is that variations in the ocean Sr/Ca ratio are small from present-day to LGM; therefore, temperature reconstructions via this method can lead to quite accurate results.

A more recent study from the work of *Tripati et al.* (in review) focuses on a new paleoclimate reconstruction method using clumped isotope thermometry

which is thermodynamically-based [15, 16, 19, 60] and founded on the principle that ordering, or clumping', of heavy isotopes into bonds with each other in molecules is temperature-dependent due to an internal isotope exchange reaction which requires no knowledge of water isotope composition [16, 19, 57]. Clumped isotope thermometry produces an LGM-Late Holocene SST change of ∼3-5°C [61].

The previous paragraphs discussed constraints on surface temperatures during the LGM. These temperatures are combined with data on the extent of tropical glaciers in order to reconstruct vertical temperature gradients and study atmospheric behavior. Changes in the freezing level of tropical glaciers have been linked to air temperatures at sea level [47]. Tropical glaciers with high amounts of precipitation in the WPWP are limited in their growth by the height of the 0°C isotherm and low seasonality of tropical climates leads to a relatively constant freezing level height [24, 28, 49]. Therefore the extent of tropical glaciers will provide the approximate height of the freezing level during the LGM providing a second data point to better understand the past vertical temperature structure of the WPWP and therefore the atmospheric lapse rate. Mid-20^{th} century snowlines for Papua New Guinea and Borneo (two islands within the WPWP) reside at ∼4600-4700m [2, 22, 35, 49, 51] above sea level whereas LGM snowlines are ∼3600-3700m [22, 49, 51] above sea level. This represents a ∼1km change in the 0°C isotherm from LGM to present.

1.4 LGM modeling efforts

This thesis presents an analysis of the atmospheric surface and vertical conditions for the model while analyzing the surface and vertical proxy thermometry available. One of the first collaborative attempts to systematically apply the same boundary conditions to different climate models and simulate past climates using state-of-the-art paleoclimate data and GCMs was the Paleoclimate Modelling Intercomparison Project (PMIP). This international project, originated in 1994, involves 18 modeling groups and is endorsed by both the International Geosphere Biosphere Project and the World Climate Research Program [27]. The goal of PMIP was to evaluate climate models under paleoclimate conditions 21,000 years BP (roughly the time of LGM) and improve the understanding of past climates [27].

The initial PMIP models ran with the following boundary conditions 21,000 years BP. SST and sea ice cover boundary conditions consisted of two experiments: one used prescribed values from the CLIMAP dataset and the other computed these values using coupled atmospheric-mixed layer ocean models and assumed no change in ocean heat transport [27]. The ice sheet volume and extent (Figure 5.4) used for the model runs, called ICE-4G, comes from the work by Peltier using a gravitationally self-consistent theory [42]. Each model implemented a 105-meter sea level reduction compared to present-day. The atmospheric CO2 concentration was lowered to 200 ppm compared to the modern era value of 345 ppm at the time of the model runs. Finally, the orbital parameter changes, albeit small, are important for radiative forcing calculations and included an increase in eccentricity from 0.016724 to 0.018994, a decrease in axial

tilt from 23.446 to 22.949, and an increase in angular precession from 102.04 to 114.42 prescribed to the reference values of 1950 A.D. [27].

The PMIP models were useful in testing the models' results compared to the proxy data and provided an insight on how the current models portray climatic conditions during the LGM. The models that used the prescribed CLIMAP SSTs showed relatively consistent mean global cooling of 4°C [27] whereas the models using the computed SST experiment showed a larger range of -6°C to -2°C (Figure 5.5). Some downfalls of the first run of the PMIP models include a lack of computer power leading to very low-resolution models compared to future LGM runs, none were fully coupled atmosphere-ocean models resulting in limited interactions between the atmosphere and ocean which has proven to be a significant process in the tropics, and PMIP did not include a vegetation component in the models producing a lack of inclusion in the large changes in vegetation and carbon cycle functions during the LGM.

After the success and knowledge gained from PMIP model runs, research priorities for the next phase were discussed during the fourth international workshop of the Paleoclimate Modelling Intercomparison Project in 2002 where the international collaborators defined several key foci for the LGM runs. The first priority was to implement coupled ocean-atmosphere (OAGCM) and ocean-atmosphere-vegetation (OAVGCM) simulations to the response of glacial conditions. The LGM experiment was to start from year 200 of the control experiment then be forced to the glacial state and then run for an additional 500 years in order to obtain changes in annual- to centennial- scale climate variability [21]. The second priority involved prescribing freshwater fluxes into the models to compare the response of coupled models to a prescribed amount and duration of freshwater

input into the high latitudes (50-70°N) of the Atlantic Ocean [21].

In terms of boundary conditions, PMIP2 lowered the concentration of CO_2 to 185 ppm and implemented two key greenhouse gases: methane (CH_4) at 350 ppb and nitrous oxide (N_2O) at 200 ppb [12, 17, 37]. The decrease in the greenhouse gases relative to the pre-industrial results in a -2.8 Wm^{-2} radiative forcing of the troposphere during LGM [5]. The ice sheet scheme used was ICE-5G, the successor of ICE-4G from PMIP, which was significantly improved from the ICE-4G scheme. The most notable improvement was ICE-5G contained considerably more mass of land-based ice, primarily as a consequence of the heavy ice cover that was added outboard of Hudson Bay [45]. All other boundary conditions did not undergo sizeable changes and were consistent with PMIP2 control runs.

The most notable difference between PMIP and PMIP2 model averages was the larger decrease in surface temperatures above the Laurentide ice sheet associated with the upgraded ICE-5G scheme. The global change in temperature between LGM and the pre-industrial era (Figure 5.6) ranges from -3.6 to -5.7°C with a tropical cooling of -2.7±0.5°C [5]. From Figure 5.6, the PMIP2 models are cooler than PMIP forced CLIMAP SST models primarily because the simulations are colder in the tropical region and across North America. However, in the Pacific Ocean the PMIP2 LGM experiments do not agree in many aspects of the signature of the SST changes [14].

For the third version of PMIP (PMIP3), two modeling communities (the Paleoclimate Modelling Intercomparison Project and the Coupled Model Intercomparison Project [CMIP]) collaborated for an increased level of model comparison and symmetry. PMIP3 and CMIP5 models are all configured with the same pre-industrial control run boundary conditions, which do not differ much from the

PMIP2 experiments. The PMIP3 LGM experiments saw noticeable changes in the ice sheet reconstruction (Figure 5.7) as it is a blended product obtained by averaging three different ice sheet reconstructions: ICE-6G v2.0 provided by Dick Peltier, MOCA provided by Lev Tarasov and ANU provided by Kurt Lambeck [46]. Many models are currently producing LGM results according to the PMIP3 experiments. Not all model averages and differences are yet available but will be for the IPCC 5^{th} Assessment Report.

Given there are over ten models incorporated into the PMIP suite, this paper will focus on the National Center for Atmospheric Research (NCAR) Community Climate System Model (CCSM). CCSM is a coupled climate model for simulating the Earth's climate system that is composed of four separate models simultaneously simulating the Earth's atmosphere, ocean, land surface, and sea-ice [62]. To date there are four main versions of this model: CCSM1.0 released in June 1996, CCSM2.0 released in May 2002, CCSM3.0 released in June 2004, and CCSM4.0 released in April 2010. The latter two versions, being the most recent, are the main emphasis of the model comparison portion of this thesis in order to determine how these models compare to paleothermometry proxy data during changes in the WPWP's climate under LGM boundary conditions.

1.5 CCSM3

CCSM3 consists of four non-coupled components simultaneously integrating forward in time, periodically stopping to exchange information with the coupler [62]. The coupler then receives fields from the component models, computes, maps, and merges this information and sends the fields back to the component models

[62]. A detailed explanation of each component model is below.

The Community Atmosphere Model version 3 (CAM3) is a dynamical, global atmospheric general circulation model developed from the NCAR CCM3 [62]. The primary resolution is 128 longitudinal by 64 latitudinal points (T42) with 26 vertical levels, however, the zonal resolution at the equator ranges depending on the grid spacing from 3.75° (T31) to 1.41° (T85) [11, 62]. In the 26 vertical levels a hybrid coordinate merges a terrain-following sigma coordinate at the bottom surface with a pressure-level coordinate at the top of the model [11, 62]. The CAM3 cloud and precipitation processes include advection, detrainment, and sedimentation of cloud condensate along with separate treatments of frozen and liquid precipitation [11]. Deep convection within the model is treated with a parameterization scheme developed by *Zhang and McFarlane* (1995) based on a plume ensemble approach where it is assumed that an ensemble of convective scale updrafts may exist whenever the atmosphere is conditionally unstable in the lower troposphere[10]. A more in-depth discussion of the entrainment process will be discussed in the Atmospheric Convection and Entrainment section. The radiation code does not incorporate the indirect effects of aerosols on cloud albedo and cloud lifetime. Improvements from the previous version, CAM2, include new treatments of cloud and ice-phase processes, upgraded representation of the interactions among water vapor, solar radiation, and terrestrial thermal radiation, new treatment of the effects of aerosols, including prognostic sulfate, on the reflection and absorption of solar radiation, and new dynamical framework suitable for modeling atmospheric chemistry [11].

The Community Land Model version 3 (CLM3) is the result of a collaborative project between scientists in the Terrestrial Sciences Section of the Climate

and Global Dynamics Division at NCAR and the CCSM Land Model Working Group [11, 62]. The CLM3 resolution is the same as CAM3 and is composed of 10 subsurface soil layers. Additionally, CLM3 represents the largest spacial patterns of sub-grid heterogeneity and includes glaciers, lakes, wetlands, urban areas, and vegetated regions [11]. Improvements to the land model, from the previous version, incorporate new methods to enable simulation of the terrestrial carbon cycle, new methods to enable simulation of dynamic vegetation, improvements in land-surface physics to reduce temperature biases, and new load balancing implementation results in substantial performance improvement [11].

The ocean model is an extension of the Parallel Ocean Program (POP) version 1.4.3 from Los Alamos National Laboratory. POP grids in CCSM are displaced-pole grids (centered at Greenland) at approximately 1°(gx1v3) and 3.6°(gx3v5) horizontal resolutions with 40 and 25 vertical levels, respectively [62]. An important aspect of POP is it does not support a slab ocean model as is supported by the stand-alone atmosphere model (CAM3) [62]. In the development of the ocean component, absorption of solar radiation in the upper ocean varies monthly and spatially based on in-situ chlorophyll and satellite ocean color observations and air-sea turbulent fluxes of momentum, heat, and moisture are computed using the wind vector relative to the ocean surface current, excluding wind gusts [11]. Upgrades to the ocean model from past versions include improvements to the representation of the ocean mixed layer, inclusion of solar heating by chlorophyll, and new infrastructure for studying vertical mixing in the ocean [11].

The sea-ice component is the Community Sea-Ice Model version 5 (CSIM5) with the same horizontal resolution as POP [11, 62]. CSIM5 includes the elastic-viscous-plastic (EVP) dynamics scheme, an ice thickness distribution, energy-

conserving thermodynamics, a slab ocean mixed layer model, and the ability to run using prescribed ice concentrations [62]. When the ice is covered by cold, dry snow, the sea-ice component albedo parameterization is biased low by about 0.07 compared to observations resulting in lower albedos and hence larger-than-observed solar radiation absorption in Polar Regions [11]. Improvements to the sea-ice model incorporate new advanced sea ice rheology, explicit ice-thickness distribution physics, explicit treatment of brine pockets, and an improved scheme for horizontal advection of sea ice [11].

Several errors and biases have been reported in CCSM3. In the tropical Pacific Ocean, CCSM3 produces a double ITCZ merging with the South Pacific Convergence Zone (SPCZ) like previous generations of the Community Climate System Model [11]. The SPCZ is a semi-permanent convection band extending from the ITCZ near the equator, around eastern Papua New Guinea, southeastward to the extratropical South Pacific (around 30°S, 130°W) [59]. A southern branch of the ITCZ replaces the SPCZ during the summer months [11, 59] causing more cloud coverage and precipitation over this region compared to observations as seen in Figure 5.8. Furthermore, Figure 5.9 shows a warm SST bias emanating from this double ITCZ in a band near 10°S in the central and eastern Pacific along with a pronounced westward expansion of the cold tongue [59]. In addition to the double ITCZ, the maximum precipitation is displaced roughly 30° to the west in the northern half of the WPWP [11] significantly changing the simulated hydrological cycle in this region (Figure 5.8).

Beyond the double ITCZ bias, CCSM3 produces warmer SSTs off of the western coasts of continents [11] mainly due to the grid resolution positioning the major areas of upwelling well off the coasts causing these regions to be substantially

warmer than observations. The model underestimates downwelling shortwave radiation in the Arctic region resulting in excess cloudiness during the winter months and an overestimate of longwave surface flux by 20 Wm^{-2}. This bias artificially increases the average surface temperature of the Arctic region during the crucially cold winter months of December to April. In the Pacific Ocean, CCSM3 does a poor job reproducing the ENSO frequency spectrum distribution [18] and produces ENSO events with very little power/energy. A final bias of CCSM3 worth mentioning is how the convection scheme used effects precipitation. The model's ability to produce large-precipitation events is well under observations causing no events with a precipitation rate above 50 mm/day [18]. The cause and implications of this effect will be reserved for the Atmospheric Convection and Entrainment section.

Following the PMIP2 boundary conditions, CCSM3 modeled the LGM with horizontal grid spacing roughly double in size (2.8125° by 2.8125° by 26 vertical levels) of the pre-industrial and future climate runs. The significantly reduced horizontal resolution resulted in the CCSM3 LGM runs to return very coarse data, which ultimately effected how well the model could simulate the LGM timeframe. More will be discussed in the Results and Discussion section on model resolution and data output.

1.6 CCSM4

The fourth version of the Community Climate System Model (CCSM4) received notable improvements in the ability to use a single code base in a start-to-end development cycle allowing higher resolutions at shorter timespans [4, 18, 36].

The major implementation of this model will be used in the IPCC 5th Assessment Report according to the CMIP5 boundary conditions and be a significant model of the PMIP3 dataset.

The Community Atmosphere Model version 4 (CAM4) has an improved horizontal resolution from CAM3 of 1.25° by 0.9° [4, 18, 36] in addition to the same 26 vertical levels in CAM3. The deep convection scheme in CAM4 saw the largest changes as it included the effects of deep convection in the momentum equation and used a dilute approximation in the convective plume calculation [18]. The enhancement results in deep convection events that occur less often but with greater intensity when compared to CAM3 [18], which is in greater agreement with observations. Additional improvements included adjusting the Arctic cloud fraction reducing low-level cloud development in the Arctic winter [18], radiation interface, and computational scalability.

The Community Land Model version 4 (CLM4) has the same resolution as CAM4. CLM4 saw the addition of a prognostic carbon-nitrogen cycle component but the carbon-nitrogen fluxes do not pass through the atmosphere and are diagnostic [18]. However, this cycle does have a seasonal and interannual vegetation phenology and upgraded urban land model which both influence regional and global climate. One of the largest changes to CLM4 is the extension of the ground column by an additional 50m depth by adding five bedrock layers [18]. Thus allowing the land model to have a larger capacity to hold moisture. A final notable improvement is the requirement of heat from the ocean component to melt ice [18] resulting in an improved global heat conservation of CCSM4 compared to CCSM3.

The Parallel Ocean Program version 2 (POP2) has a uniform zonal resolution

of 1.11° and a meridional resolution of 0.27° around the equator that gradually increases to 0.54° at 33°N/S and stays constant beyond these latitudes toward the poles. The number of vertical levels increased from 40 in CCSM3 to 60 in CCSM4 with a higher resolution of the upper ocean. The vertical mixing equations added a term that is proportional to the tidal energy allowing a little more cross isopycnal mixing in the deep ocean [18].

The sea ice component, Community Ice Code version 4 (CICE4), incorporates a new radiative transfer scheme, which uses inherent optical properties to define the scattering and absorption characteristics of snow, sea ice, and included absorbers [18]. The updated scheme gives CCSM4 more realistic surface ice albedos compared to the biased lower albedos of CCSM3. The LGM run of CCSM4 maintains the same horizontal and vertical grid resolution as the pre-industrial control run. This allows for a much enhanced topology resolution, which is important for the LGM as a large portion of the WPWP was above water during this time period as a result of the emergence of the Sahul Shelf from Australia to Southeast Asia. Additionally, the upgraded grid resolution provides greater replication of mountains, coastlines, and overall provides a better representation of LGM boundary conditions (to be explained in the Results section) compared to the CCSM3 LGM run.

One difference between CCSM3 and CCSM4 is the initial year of the pre-industrial control run, 1870 and 1850 respectively. The pre-industrial control run is a long integration where model boundary conditions are held constant to provide a means to understand the basic climate of the model. 1850 (CCSM4) was chosen instead of 1870 (CCSM3) as the initiation year because the CO_2 and aerosol concentrations are closer to pre-industrial levels in 1850 [18]. This

makes it more difficult to compare the CCSM3 and CCSM4 pre-industrial control runs, however, CCSM4 has a more realistic 20^{th} century run when compared to the observations, where the climate system, including the ocean component, is gaining heat [18] as opposed to losing heat as seen in the CCSM3 runs. For simplicity, this thesis will only focus on the LGM and pre-industrial control runs of CCSM3 and CCSM4.

With the aforementioned improvements, CCSM4 overall does improve with respect to pre-industrial observations. From the pre-industrial control runs, the mean SST difference from the *Hurrell et al.* (2008) observations in CCSM4 is 0.1°C compared to -0.8°C for CCSM3, with root-mean-square errors (RMSE) of 1.1° and 1.6° respectively [18]. From Figure 5.10, it is evident that the eastern and western ocean boundaries are still warmer than observations, however, the large amount of cooling seen in the Pacific and Southern Oceans of CCSM3 is not as evident in CCSM4 causing an overall global agreement of SSTs. It is good to keep in mind CCSM4 regionally has deficiencies but matches the global ocean temperature observations much better than CCSM3. The enhanced mean SSTs of CCSM4, to a large degree, can be attributed to the higher resolution of the model. There is a better representation of topography due to the increased resolution causing the atmosphere component to produce stronger upwelling-producing winds located along CCSM4 western boundary coasts rather than somewhat offshore as seen in CCSM3 [18].

To fully understand each of the models' climate states under the influence of boundary conditions, the 20^{th}-century run needs to be briefly analyzed. The global land surface temperature mean bias decreased in CCSM4 to -0.2°C from -0.3°C in CCSM3 from the observations for the twentieth-century runs with root-

mean-squared errors of 2.7°C and 3.01°C, respectively [18]. From Figure 5.11, one can see the improvement is not as obvious by just looking at the figure. CCSM4 shows a much warmer sector of Eastern Europe and Russia (warmer than observations) during the 20th-century run which ultimately added to the decrease in the mean absolute temperature bias, however, the RMSE did decrease as well meaning overall the model is in better agreement with the observations than CCSM3.

The Pacific Ocean SSTs in CCSM4 are slightly warmer (<0.4°C) than observations which is a significant improvement to CCSM3 Pacific Ocean temperatures of 1.5°C colder [18]. Both the western and eastern boundaries in the Pacific Ocean are too warm in each model version [18]; however, a notable improvement with CCSM4 is the reproduction of ENSO. CCSM3's ENSO events were overly regular at 2-year periods [11, 18] and are in drastic contrast with observations of peak variability between 3 and 7 years. The SSTs across the tropical Pacific Ocean in CCSM3 were poorly represented due to the failure of ENSO variability; hence a major focus of CCSM4 was to greatly improve this variability. CCSM4 ENSO events have very little power at 2 years and variability between 3 and 6 years with a peak at 4 years [18]. This improvement was a result of the two changes to the CAM4 deep convection scheme [18] documented in *Richter and Rasch* (2008) and *Neale et al.* (2008). However, the CCSM4 ENSO variability is not perfect as the amplitude is much greater than the *Hurrell et al.* (2008) observational dataset [18]. Beyond the increased amplitude, CCSM4 does a decent job replicating the 20^{th}-century variability, has a more realistic width to the positive correlations in the central and eastern tropical Pacific Ocean [18] and the horseshoe pattern of negative correlations in the western tropical Pacific that stretches into the

midlatitudes of both hemispheres is greatly improved [18].

CCSM4 has many improvements from CCSM3 as discussed above, however, there still exist areas that will continuously need fine-tuning and enhancements within the next version. The first significant bias is the double ITCZ formation in the western Pacific Ocean leading to biased precipitation and temperature throughout the entire year [4, 18]. Although, the double ITCZ in CCSM4 is improved from CCSM3, it needs additional enhancements to accurately match observational data. The Arctic region still exhibits too much low cloud coverage [18], which increases the overall surface temperature. Another bias is the strong surface temperatures over continents (most notably Eastern Europe/western Russia) where some regions are greater than 2°C compared to observations [18]. The exclusion of the effects of indirect aerosols in CCSM4 is very likely a major factor causing the larger increase in globally-averaged surface temperatures over the 20^{th}-century runs compared to the observations [18] in addition to an ocean heat uptake that is too small or the model climate sensitivity is too large [4, 18].

1.7 Atmospheric Convection and Entrainment

One of the most significant enhancements pertaining to the WPWP from CCSM3 to CCSM4 is the updated entrainment scheme [18, 38, 54]. Inclusion of entrainment in deep convective plumes is an important process of the WPWP and therefore an imperative component of this research. From *Richter and Rasch* (2008), convection is one of the most important processes driving tropospheric circulation as it distributes heat and moisture and transports constituents and momentum.

Prior to a discussion on the changes of the entrainment scheme, an analysis

of atmospheric convection processes is useful. As a parcel of air warms up at the surface it becomes less dense than the environmental air surrounding it resulting in an upward vertical force against the parcel. As the unsaturated parcel rises its temperature decreases at the dry adiabatic lapse rate ($\sim$10°C per kilometer) until it reaches saturation at the level known as the lifting condensation level (LCL). Beyond the LCL a parcel theoretically rises at the moist-adiabatic lapse rate ($\sim$6.5°C per kilometer as latent heat is released due to conversion of water vapor into liquid water) until the parcel is no longer buoyant. The role of entrainment is implemented because the upward moving air parcel is not a closed system therefore the air parcel properties will mix with the surrounding environmental properties (typically lower temperature and drier air). The entrainment of drier air causes the air parcel to be undersaturated with respect to its environment thus increasing its lapse rate away from the hypothetical moist-adiabatic lapse rate subsequently cooling the parcel at a faster rate. In addition to cooling the air parcel at a faster rate, entrainment also creates an unstable environment for the rising parcel consequently enhancing deep convection. This has been demonstrated in recent observations [7, 23, 26, 58] and modeling studies of modern datasets [29, 38, 56, 61] showing that moist convection has a strong dependence on free tropospheric humidity that occurs via entrainment of air into the convecting parcel. In addition, it has been shown that factors such as the onset of precipitating deep convection and cloud top height can only be matched if substantial entrainment is considered [7, 23, 26, 58, 61]. A crucial part of this thesis and the effect of entrainment centers on how entrainment affects the freezing level in the atmosphere. Deviations of a parcel's lapse rate become important when analyzing the vertical temperature structure and freezing level (model based) to

the collected paleoclimate proxy data freezing level (snow line data).

In CCSM3 the process of deep convection is treated with a parameterization scheme developed by *Zhang and McFarlane* (1995). Based on a plume ensemble approach where it is assumed that an ensemble of convective scale updrafts may exist whenever the atmosphere is conditionally unstable in the lower troposphere [10]. Moist convection occurs only when there is convective available potential energy (CAPE) for which parcel ascent from the sub-cloud layer acts to destroy the CAPE at an exponential rate using a specified adjustment time scale [10]. With the parameterizations it is important to note the cloud base, any inhibitions to atmospheric ascent, and the amount of CAPE (larger CAPE corresponds to larger atmospheric instabilities). CCSM3 plumes that carry mass upward are detrained into the environment in a thin layer at the top of the plume where the detrained air is assumed to have the same thermal properties as in the environment [10]. All condensation is assumed to occur within the updraft plumes and each plume is assumed to have the same value for the cloud base mass flux. The total entrainment rate is given by the change in mass flux and the total detrainment [10]. The entrainment process is halted once the convective cumulus clouds consume the entire CAPE.

Changes to the process of deep convection in CCSM4 include the addition of convective momentum transports by *Richter and Rasch* (2008) and a modified dilute plume calculation following *Raymond and Blyth* (1986, 1992) [39]. Convective momentum transport must be parameterized as convection itself is parameterized, however, the largest uncertainties come from the need to estimate in-cloud horizontal velocities [54]. Increasing the horizontal in-cloud convergence will lead to increased vertical velocity and hence deeper convection. The in-

clusion of this parameter in CAM3 and CAM4 strongly influences near-surface winds as well as the distribution of convection in the tropics [54]. The convective momentum transport parameter improved model wind biases over the tropics resulting in better Hadley circulation representation [54]. *Neale et al.* (2008) concluded that including convective momentum transport in the convection parameterization weakened the trade winds and the off-equatorial wind response to an ENSO event; allowing for convective plume entrainment strengthened by Madden-Julian Oscillation activity. The first process increased the period of ENSO events in CCSM4 and the second process added a mechanism for maintaining ENSO events [38]. Thus significantly improving the variability of ENSO and representation of SSTs, winds, and precipitation across the tropical Pacific Ocean and more specifically the WPWP in addition to better representing convective activity.

From the work by *Raymond and Blyth* (1986, 1992), CCSM4 tuned the dilute plume calculation, which represents when vertically transported liquid water is converted to ice/freezing water. This is a significant component of deep convection and enhances entrainment as freezing of liquid water and unloading of precipitation can significantly increase the buoyancy of updrafts, up to the equivalent of 3°C at the -15°C level as shown in their model [53]. When dealing with available convective energy, small increases in buoyancy can amount to large increases in the amount of parcel-environment entrainment and thus large changes in the height of the freezing level.

CHAPTER 2

Methods

2.1 Constraining present-day mean vertical temperature profiles in the WPWP

One part of this thesis focuses on obtaining the accurate mean vertical atmospheric temperatures in the WPWP in collaboration with Sandeep Sahany. The aim was to determine on average how close does the vertical structure of the atmosphere in the WPWP follow a moist adiabatic lapse. Given the WPWP's abundance of water vapor and convection, a lapse rate close to moist adiabatic has always been assumed. To obtain a better understanding of the WPWP processes, sounding data was collected over Manus, Papua New Guinea (2° 3' 39.64" S, 147° 25' 31.43" E) and Nauru Island (0° 31' 15.6" S, 166° 54' 57.60" E) from archived data of the U.S. Department of Energy as part of the Atmospheric Radiation Measurement (DOE ARM) Climate Research Facility. The importance of the sounding data is to diagnose the average vertical profile over the two locations in order to better interpret the surface temperature, surface and free tropospheric relative humidity, and temperature lapse rate in the WPWP.

When comparing the sounding data of Manus and Nauru to the observed present-day glacial extent in the WPWP, it is evident the 0°C isotherm in the

sounding data is ∼500m above the average tropical glacier extent for the middle of the 20^{th} century. This discrepancy is attributed to depression of tropical glacial equilibrium line altitudes to the 1°C isotherm, and the different time intervals sampled by the sounding data and the snowlines given the influence of anthropogenic warming [49, 50, 61]. For simplicity we assume a similar or smaller offset between glacial snowlines and the height of the atmospheric freezing level at the LGM.

2.2 Applying an entraining plume model to study the modern and LGM eras

The second part of this research employs a radiative-convective model [56], created by Sandeep Sahany based on convective plume computations from *Holloway and Neelin* (2009), with entrainment sensitivity to analyze the present-day and LGM vertical temperature profile sensitivities. This model is a relatively simple model much like the moist adiabat approach; however, it takes into account the influence of entrainment of the environmental air in the free troposphere. The model is more complex by designating air temperature and relative humidity as a function of height in order to evaluate the sensitivity [7, 23, 26, 58] of each parameter: surface air temperature, surface relative humidity, free tropospheric relative humidity, and entrainment rate. Therefore the parcel, with specified surface conditions, is forced to rise at the dry adiabatic lapse rate until saturation thereafter rising at a modified lapse rate. The paper by *Tripati et al.* (in review) explains that the environmental temperature above this boundary is calculated as a modified radiative-convective equilibrium using a Betts-Miller convective

scheme that adjusts the large-scale temperature towards that of the entraining convective plume. The cooling term (which can include a large-scale dynamical component) is approximated as independent of height in the lower free troposphere. Standard case cooling of 1.5°C/day and Betts-Miller 0.1-day convective time scale yield a single combined parameter of a 0.15°C difference between environment and convective plume temperature. This is the best and most direct approach for the highly convection WPWP allowing for a further understanding of how small changes in climatic variables can adjust the 0°C isotherm in the atmosphere. For a more detailed description of the model please reference *Tripati et al.* (in review).

The radiative-convective model was employed to obtain a best-fit of the average lapse rate over Manus and Nauru to the model's lapse rate. Because entrainment is strongest during times of convection, the soundings used were those with at least a minimum level of precipitation (0.005 mm/h average from one-minute resolution optical gauge data) over a three-hour window about the sounding time [61]. Additionally, the one piece of the model missing was the relative humidity of the free lower troposphere, which is the region above the boundary layer. The free tropospheric relative humidity is a vital piece of the puzzle as it represents the saturation level of the environmental air being entrained into a parcel. Therefore, the drier the free tropospheric air then the steeper the lapse rate as the parcel is drying out slowly as it rises. In order to accomplish this, the model was configured with a present-day surface temperature of 28.8°C, surface relative humidity of 81%, and an appropriate entrainment rate for the highly convective WPWP. The model lapse rate, which matched the present-day sounding dataset best, had a free lower tropospheric relative humidity of 76%. The four above-

mentioned values will be considered the base values and sensitivity tests will be applied in relation to these values.

Through this model, small variations in the aforementioned parameters are changed to represent a plausible LGM scenario based on proxy data surface temperatures and freezing level changes. Sensitivity tests were also performed to determine the change in freezing level height corresponding to changes in the specified parameters. This method gives reasonable ranges of change in surface temperature and surface relative humidity for the LGM providing an upper and lower limit in which one would expect the GCMs to fall within. From the work by *O'Gorman and Muller* (2010), the WPWP has a ∼0.5% change in surface relative humidity and a ∼1-1.5% change in relative humidity at 500hPa (free troposphere) for a 1°C change in temperature. This will become an important range of plausible changes in atmospheric variables for the sensitivity tests discussed in the Results section.

2.3 CCSM analysis

The Community Climate System Model analysis is the final focus and main emphasis of the thesis. This research was granted early access to several key CCSM4 model runs and manuscripts thanks to Bette Otto-Bliesner, Senior Scientist in the Paleoclimate Group in the Climate and Global Dynamics Division at the National Center for Atmospheric Research in Boulder, Colorado. Analysis of CCSM3 and CCSM4 has several different parts: the pre-industrial (PI) control run, the LGM run, and the difference between the LGM and pre-industrial runs. For each specific run, several variables are analyzed which include the fraction of

land above water, temperatures at the surface, 600hPa, and 510hPa along with vertical temperature profiles, precipitation rate, prescribed evaporation rate from model latent heat flux, and wind/streamlines near the surface and 510hPa. The mid-level analysis at 600hPa and 510hPa was selected, as these are the closest atmospheric levels associated with the models' 0°C isotherm for the LGM and PI runs, respectively. The 600hPa level corresponds to a height above sea level of 4347m for CCSM3 LGM, 4329m for CCSM4 LGM, 4378m for CCSM3 PI, and 4351m for CCSM4 PI. The 510hPa level corresponds to a height above sea level of 5634m for CCSM3 LGM, 5615m for CCSM4 LGM, 5679m for CCSM3 PI, and 5650m for CCSM4 PI. The grid box used to represent the WPWP consists of the region bounded by 15°S-15°N and 130°E-165°E. These coordinates were selected as they encompass the paleoclimate proxy data locations and allow for a large enough region to view outside processes that may be influencing the climate of the WPWP (Australian continent influence, Sahul Shelf emergence, and mid-latitude and central Pacific atmospheric transport). In order to look at outside atmospheric transport of water vapor or dry air, the coordinate region was expanded for the streamline analysis to 40°S-40°N and 40°E-100°W and a transport streamline tracer analysis started at four locations: 15°N, 165°E; 0°, 165°E; 15°S, 165°E; 15°S, 150°E. The transport streamline tracers for the extended region started at 20°N, 140°W and 20°S, 140°W. The vertical temperature profile was analyzed at two locations with one representing the open ocean with proximity to one of the proxy data locations (1.4°N and 146°E) and the second above the island of New Guinea (5°S and 140°E).

The PI run provides a baseline for the model's overall performance and allows understood model biases to be developed prior to analyzing the LGM runs. How-

ever, it is important to keep in mind the biases each model produces during the PI run as these will continue to plague the model for the LGM run and may even increase in magnitude during times of extreme climate conditions. The LGM run shows how the model reacts to different boundary conditions as specified earlier and represents the basis for comparison to the paleoclimate proxy data. Many factors can influence each of the variables listed, however, the much higher horizontal resolution of CCSM4 seems to be the dominating aspect as will be discussed further in the Results section. The final and most important model analysis takes the difference between the LGM run and PI run for each model. This shows each model's sensitivity to the LGM boundary conditions and allows further analysis on whether or not the model is replicating atmospheric processes that seem feasible and fundamentally sound. One issue with the CCSM3 model is the different horizontal resolutions between the LGM and PI runs. In order to get around this the PI run was regrid onto the LGM grid. This resulted in a loss of the PI run's spatial resolution in order to match that of the LGM run, but still allowed for a high enough resolution for analysis and conclusions to be made between CCSM3 and CCSM4.

For each model the monthly values during the last 50 years of the PI and LGM runs were analyzed to ensure the model was properly spun up and in a state of equilibrium under the prescribed boundary conditions. This also minimizes potential biases at the beginning of the model run as it approaches a steady state. The PI run of CCSM3 timeframe is from 500/01 (model year/model month) to 549/12 and the LGM run is from 481/01 to 530/12. The PI run of CCSM4 is from 1251/01 to 1300/12 and the LGM run is from 1452/01 to 1501/12. By using the last 50 years, the research is able to retain consistency with each models' results.

CHAPTER 3

Results and Discussion

3.1 Present-day mean vertical temperature profiles in the WPWP

From the sounding data of Manus and Nauru, it was clear by superimposing moist-adiabatic lapse rates over the vertical temperature soundings that on average the WPWP does not follow a moist adiabat. However, it is still necessary to use the present-day conditions to calculate the freezing level from a moist adiabat approach in order to show the inconsistencies between the moist adiabat and observational data.

Using a present-day SST of 28.8°C and near-surface relative humidity of ∼81%, a rising parcel becomes saturated at ∼600m above ground level under the modern adiabat approach. Beyond the point of saturation the parcel continues to rise under moist adiabatic conditions until the freezing level is reached at 6000m which is much higher than the 5200m average of the sounding data and the glacial extent data (∼4700m). The greater-than-expected value is a result of the lack of dry air entrainment in the moist adiabatic approach resulting in a relatively lower lapse rate and higher freezing level. Doing the same analysis for an LGM surface temperature reduction of 2°C, 3°C, and 4°C results in absolute

freezing levels of ∼5400m, ∼5000m, and ∼4750m respectively. Therefore, the adiabatic approach gives too large of absolute freezing levels during the modern and LGM periods concluding that this approach is not a good model for predicting the absolute freezing height in the WPWP. With the understanding that the moist adiabat approach overestimates the height of the freezing level, it is still beneficial to examine the change in freezing level with changes in surface temperature.

To match the absolute heights of the glacial extent at the LGM (assuming the glacial snowlines are within 500m of the value) using the radiative-convective model the change in the absolute freezing levels of modern data and LGM paleoclimate data were considered. This change in freezing level was calculated as the modern (4600-4700m) minus the LGM (3600-3700m) and estimated to be 900-1000m [61]. Therefore allowing much simpler sensitivity tests to be performed on the radiative-convective model to match the change in freezing level to see how small changes in atmospheric variables change the freezing level.

In order to match the change in freezing level from the present-day to the LGM, a 3°C surface temperature change corresponds to a freezing level decrease of 925m which lies within the estimated range of 900-1000m [61]. Going to a 4°C surface temperature change results in a 1215m freezing level change which is beyond the estimated LGM range but inside the bounds of the paleoclimate data [61]. If one were to estimate the LGM change in surface relative humidity required for an adiabat to match the glacial snowline data, the reductions would be ∼27%, ∼22%, ∼16%, and ∼10% for surface temperature reductions of 2°C, 3°C, 4°C, and 5°C respectively [61]. Therefore, in order to match the LGM snowline data in the WPWP using a moist adiabat, unrealistic deviations from

the estimated surface relative humidity need to be invoked.

3.2 Applying an entraining plume model to study the modern and LGM

The radiative-convective model (discussed above) was employed to obtain sensitivity tests of changes in the surface air temperature, surface relative humidity, and lower free tropospheric relative humidity corresponding to changes in the height of the freezing level. The point of the sensitivity tests is to gain an understanding of how smaller changes in atmospheric conditions can affect the freezing level height. This procedure is as close as feasible to the simplicity of the moist adiabat but takes into account the impact of entrainment of environmental air in the troposphere [61]. All of the atmospheric variables were set to present-day values and the variable under investigation was changed to analyze specific sensitivities. The sensitivity tests were as follows: a 1°C decrease in surface temperature resulted in a 235m decrease in freezing level height, a 1% decrease in surface relative humidity resulted in a 40m decrease in freezing level height, and a 1% decrease in the lower free tropospheric relative humidity resulted in a 25m decrease in freezing level height [61]. To obtain the LGM freezing level decrease of ∼900-1000m exclusively from the surface temperature, it would have had to decrease by ∼3.8-4.3°C which is a plausible range compared to the thermodynamic proxy data discussed earlier. Relying on changes in relative humidity at the surface or the free troposphere alone are too large to be plausible for a cause of the decrease in freezing level, as their changes would be 22.5-25% and 36-40%, respectively [61]. Realistically the changes in atmospheric variables are

not mutually exclusive therefore combining the sensitivity tests together gives a more informative result to changes in the WPWP during the LGM. An equation of surface temperature change corresponding to vertical freezing level change and changes in relative humidity due to temperature changes from research by *O'Gorman and Muller* (2010) can be created from the sensitivity tests:

$$\Delta H_{fl} = (235\frac{m}{T} * T) + (0.5\frac{\%}{T} * 40\frac{m}{\%} * T) + (1\frac{\%}{T} * 25\frac{m}{\%} * T)$$

$$\Delta H_{fl} = 280\frac{m}{T} * T$$

where ΔH_{fl} is the change in the freezing level, T is surface temperature change in degrees Celsius and the brackets represent freezing level height changes due to surface temperature, surface relative humidity, and free tropospheric relative humidity; from left to right.

Since large changes in the relative humidity of the surface and free troposphere are unlikely during the LGM [40], matching ΔH_{fl} with 900-1000m gives surface temperature changes of 3.2 and 3.6°C, respectively. Based on the radiative-convective model with an entrainment scheme, the LGM surface temperature was ∼3.5°C cooler than present-day which falls within the range of the proxy data. This places a very large emphasis on the freezing level reduction on changes in surface temperature and not changes in relative humidity either at the surface or in the free troposphere indicating that the LGM WPWP was much cooler than present-day [61].

3.3 CCSM analysis

Prior to analyzing the WPWP, the global perspective of CCSM3 and CCSM4 is relevant in understanding how the modeled Earth was different during the LGM according to the CCSM. This analysis is an average of monthly data over each model runs' last 50 years as noted in the Methods section. From Figure 5.12, it is evident global surface temperature change was larger in CCSM3 over the high latitude Atlantic and Southern Ocean whereas continental temperatures do not have any significant changes between the two model versions. The LGM tropical Pacific Ocean cooling is greater from the central Pacific Ocean to the coast of South America in CCSM4, but subtropical surface temperature changes are larger in CCSM3 as evident in Figure 5.12. The higher magnitude changes over the oceans in CCSM3 contributed to the LGM-PI magnitude skin temperature change being larger in CCSM3 with -5.5°C compared to -4.5°C in CCSM4. There are stark differences from the precipitation rate anomalies between the two model versions (Figure 5.13). CCSM3 tends to produce more LGM precipitation in the central Pacific Ocean and around Antarctica whereas CCSM4 produces less LGM precipitation over the same spatial area. On average, the precipitation rate change between the two models is not significant and robust in magnitude with LGM-PI changes of -0.35 mm/day and -0.28 mm/day, CCSM3 and CCSM4 respectively. From the larger temperature and precipitation changes, CCSM3 is more sensitive to LGM boundary conditions than CCSM4 on the global scale.

It is beneficial to diagnose the models' differences in order to determine if the model has undergone improvements in the WPWP for the LGM simulations. The key results for the model runs and differences are noted in Table 3.1. CCSM3

Model Comparison Results						
	CCSM3			CCSM4		
	LGM	PI	LGM-PI	LGM	PI	LGM-PI
Surface Temp (°C)	25.9	27.9	-2.0	26.0	28.0	-2.0
600hPa Temp (°C)	0.2	2.9	-2.7	-0.1	2.1	-2.2
510hPa Temp (°C)	-6.5	-2.7	-3.8	-6.9	-4.0	-2.9
Precip Rate (mm/day)	6.5	6.8	-0.3	6.9	7.1	-0.1
Evap Rate (mm/day)	4.2	4.4	-0.2	4.2	4.5	-0.3
Land Above Sea Level	15.8%	9.4%	6.4%	18.9%	9.1%	9.8%
Freezing Height (m)	4345	5031	-686	4247	4731	-484

Table 3.1: Model Comparison Results for CCSM3 and CCSM4 for the domain of the WPWP region.

indicates the WPWP cooled by ∼2.0°C at the LGM and CCSM4 results showed a similar surface cooling of 2.0°C, which are both less than the more recent paleothermometry records and radiative-convective model but lie within the range of all paleoclimate data. Freezing level (0°C isotherm) reductions were 686m for CCSM3 and 484m for CCSM4, however these reductions are not as large as the ∼900-1000m reductions in the paleoclimate glacial extent record. Additionally, the freezing level heights (Table 3.1) are higher than the paleoclimate record (∼3600-3700m for LGM and ∼4600-4700m for modern era) in all models except the CCSM4 PI run where the model comes relatively close to replicating the data snowline data.

The resolution difference between CCSM3 and CCSM4 is shown in Figure 5.14. The lower resolution CCSM3 PI and LGM runs and the higher resolution CCSM4 PI and LGM runs have an area averaged fraction of land above water in the WPWP of 0.1 for the PI and 0.2 for the LGM. The difference between the LGM and PI model runs for CCSM3 and CCM4 is both ∼0.1, however, CCSM4 has 3.4% more land above sea level in the warm pool. Both models clearly repre-

sent the emergence of the Sahul Shelf between Australia and Papua New Guinea (PNG), however, CCSM3 does not completely represent PNG's coastal boundaries and islands toward the east. Even with the much smaller grid spacing of CCSM4 the model still does not show all islands that are present with today's sea levels. An additional note is the vertical extent of the topography is larger in CCSM4 than CCSM3 over the mountain islands, specifically PNG as evident in the surface pressure (Figure 5.15).

Each pressure level below the PNG mountain surface pressure undergoes interpolation of all model variables to sea level. The lowest PNG surface pressure in CCSM3 PI is 940hPa, CCSM3 LGM is 970hPa, CCSM4 PI is 890hPa, and CCSM4 LGM is 885hPa. To no surprise the higher resolution CCSM4 represents the highest peaks of PNG (Figure 5.15) much more accurately not only resulting in lower surface pressure but also lower surface temperatures as discussed in the forthcoming temperature gradient analysis.

The change in surface temperature in the WPWP from the PI to LGM is $\sim$2.0°C for CCSM3 and CCSM4 which is significantly smaller than the cooling seen from paleothermometry. The WPWP's average surface temperature for the CCSM3 PI run is 27.9°C and 25.9°C for the LGM run, whereas for the CCSM4 PI run it is 28.0°C and 26.0°C for the LGM run. From Figure 5.16, it is evident most of the CCSM3 LGM cooling in the WPWP is coming from north of the equator where there is a large area of -2.5 to -2°C temperature changes whereas CCSM4 exhibits a smaller cooling in this region of -2 to -1.5°C. Notable features of the CCSM3 difference plot includes the smaller amount of cooling (-1.5 to -1°C) just south of the equator into the Pacific Ocean, significant cooling ($\sim$ -4°C) south of PNG where the Sahul Shelf was above water during the LGM,

and small amounts of cooling (-2.5 to -1.5°C) over the land areas of PNG and northern Australia. Overall, the differences in CCSM3 appear to be scattered and not representative of homogenous oceanic or land-based cooling, but instead are heterogeneous in structure as characteristic of the varying degrees of cooling from the land to the equator and up toward the subtropics. In contrast, the CCSM4 LGM-PI differences are much more uniform as a majority of the cooling above the ocean is between -2 to -1.5°C. As land is approached the temperature gradually increases in cooling to the point where the Sahul Shelf has a temperature difference greater than -4°C which was expected as this region is going from warm ocean temperatures to a land surface. The increased resolution of CCSM4 is noticeable in the representation of cooling on and around PNG of -3 to -2.5°C as compared to the heterogeneous cooling around PNG in CCSM3. From this comparison it is clear that CCSM4's resolution allows the model output to be smoother, but in doing so places much cooler regions where land is located and does not cool the open ocean as much as CCSM3 or research results from proxy data.

The 600hPa LGM temperature departures from PI runs for CCSM3 and CCSM4 are -2.7°C and -2.2°C, respectively. The temperatures for the LGM runs at the 600hPa level are 0.2°C for CCSM3 and -0.1°C for CCSM4 whereas 2.9°C for CCSM3 PI and 2.1°C for CCSM4 PI. It is clear both LGM and PI runs of CCSM4 are cooling faster vertically than the CCSM3 runs which is a consequence of the enhanced entrainment scheme implemented in the CCSM4 runs. From Figure 5.17, it can be seen that the CCSM3 differences are not uniform and range from -3 to -2°C across the open ocean, -2 to -1.5°C over the western mountains of PNG, and greater than -3°C as one moves toward the subtropics

(15°N/S). CCSM4 differences do not illustrate a large separation of temperatures and instead vary between -2.5 to -2°C except for regions above land (-3 to -2.5°C) where the temperature difference is slightly larger. The major difference between model 600hPa (∼freezing level) temperatures is a more uniform structure in CCSM4 whereas CCSM3's cooling can be split up into zonal bands from the equator to the subtropics.

The 510hPa LGM temperature departures from PI runs for CCSM3 and CCSM4 are -3.9°C and -2.9°C, respectively. This continued the trend of CCSM4 cooling faster than CCSM3 where at 510hPa the temperatures across the WPWP were as follows: -2.7°C CCSM3 PI, -6.5°C CCSM3 LGM, -4.0°C CCSM4 PI, and -6.9°C CCSM4 LGM. It is important to note the CCSM4 LGM surface temperature was larger than CCSM3 LGM so therefore the change with pressure is greater for CCSM4 than it is for CCSM3. From Figure 5.18, the zonal temperature structure of CCSM3 is lost slightly where the open ocean difference is -4 to -3.5°C and over the Sahul Shelf it is -4.5 to -4°C. CCSM4 has a uniform temperature structure from the open ocean (-3 to -2.5°C) to over land (-3.5 to -3°C) which physically makes sense as the land temperature will decrease faster due to the lack of water vapor compared to the open ocean region.

The surface temperature gradient in the WPWP, which is the temperature change from the surface of the PNG mountains to the surface temperature directly above the equatorial ocean waters northeast of PNG showed large changes between models and scenarios. For each model run, the 50-year average surface temperature of the two locations was analyzed and compared between model runs. The CCSM3 PI run's PNG mountain temperature is 25°C and the temperature above the ocean is 28.5°C representing a temperature gradient of 3.5°C.

In comparison, the CCSM3 LGM run's PNG mountain and ocean temperatures are 21.5°C and 27°C, respectively, leading to a 5.5°C temperature gradient. This mountain-to-ocean surface temperature gradient is more evident in the CCSM4 model runs. The PNG mountain surface temperature is lowest at 20°C and above the ocean the temperature is 29°C corresponding to a temperature gradient of 9°C for the CCSM4 PI run. The CCSM4 LGM run shows the largest mountain-to-ocean temperature gradient of 10°C where the PNG mountain and open ocean temperatures are 27°C and 17°C, respectively. From this analysis, it is clear the enhanced topography and spatial resolution of CCSM4 resulted in a larger mountain-to-ocean temperature gradient, as the PNG mountain temperature is much lower in CCSM4 than CCSM3. The mountain-to-ocean surface temperature gradient in the WPWP at 600hPa (Table 3.2) is similar to the results at the surface except for each model run the 600hPa magnitude is smaller. The gradient is smaller in the CCSM3 LGM run than the PI run which is a reversal of the surface gradient. The CCSM4 runs have larger temperature gradients than CCSM3 over PNG, which may have initialized from a mountain boundary layer that is persistent to unreasonable heights above the PNG mountain range due to the higher topographic resolution of CCSM4 compared to CCSM3. NCEP reanalysis over the WPWP shows the temperature converging between the ocean and area above PNG to a homogenous temperature as seen in Figure 5.19 taken from *Tripati et al.* (in review), therefore demonstrating an area of weakness in the model temperature simulation. Similarly, the 510hPa mountain-to-ocean surface temperature gradient is still evident and increased in the CCSM3 PI (3°C), LGM (2.5°C), and CCSM4 PI (5°C) runs but stayed at 5.5°C for the CCSM4 LGM run. This is as expected since the 510hPa and 600hPa levels are spatially close,

600hPa Mountain-to-Ocean Temperature Gradient			
Model Run	PNG Temp (°C)	Ocean Temp (°C)	M-O Gradient (°C)
CCSM3 PI	2.8	0.5	2.3
CCSM3 LGM	0.2	-1.2	1.4
CCSM4 PI	2.0	-2.5	4.5
CCSM4 LGM	0.0	-5.5	5.5

Table 3.2: The temperature gradient for each model runs at 600hPa from above PNG to the open ocean northeast of the island denoted as PNG and Ocean, respectively, in the table. M-O is the temperature gradient (°C) calculated as 600hPa PNG Temperature minus the 600hPa Ocean Temperature.

however, it is interesting as to why the CCSM3 LGM gradient increased by 1°C between the two levels. Prior knowledge and NCEP reanalysis data show relatively homogenous temperatures at higher levels of the troposphere above land and ocean surfaces (Figure 5.19). Finally, the 510hPa and 600hPa levels represent the atmospheric freezing level for the PI and LGM scenarios, respectively. For the two pressure levels and each model version/run, a range of 1.5-5.5°C for the temperature difference between the mountains and ocean regions corresponds to a 230-850m freezing level difference assuming a moist adiabatic lapse rate of 6.5°C/km. This difference falls in line with the ∼500m discrepancy between the 0°C isotherm derived from sounding data in the WPWP and the tropical glacial extent in PNG as discussed in the methods section leading to a possible explanation to the aforementioned difference.

The vertical temperature structure above PNG and the proxy location (discussed in the Methods section) for both CCSM3 and CCSM4 in Figure 5.20 shows the much cooler surface temperatures for PNG in CCSM4. There are large changes in the lower troposphere; however, the changes in the upper troposphere are negligible. The CCSM3 LGM temperature structure over the open ocean is

similar to that of the PI run's structure over PNG as illustrated at pressure levels below 510hPa, however, the CCSM4 model runs depict temperature structures that are not aligned. This is due to the fact that the surface temperature between the two regions is significantly different allowing no merge in the lower or upper troposphere thus leading to a heterogeneous model vertical temperature structure between the two areas. The temperature profiles at the surface and the majority of the lower-troposphere are farther apart in CCSM4 whereas CCSM3 temperature profiles are very close (Figure 5.20) indicating more sensitivity in CCSM4. The CCSM3 LGM-PI (Figure 5.21) shows that for a majority of the vertical extent the temperature difference is largest over the open ocean proxy site and smaller over PNG. However, the opposite is true for the CCSM4 runs where the differences are much larger over PNG for all pressure levels except for 710hPa indicating that the cooling during the LGM is larger over land surfaces throughout the entire extent of the lower troposphere in the WPWP.

This could be the link between the discrepancies of the present-day glacial extent observation records and the freezing level in the sounding data. The false mountain boundary layer as seen in both CCSM3 and CCSM4 extends all the way up to the upper-levels of the troposphere which is realistic near the mountain but should diminish in effect as the mountain peak is surpassed. From NCEP reanalysis data, the temperature difference above a mountain and the open ocean decreases with increasing height, however both models retain some amount of temperature gradient. This leads to a possible flaw in the models' handling of mountain boundary layers in the vertical extent which could be caused by model numerical treatment around mountains, interaction with the convective scheme, or an error from interpolating sigma coordinates to pressure coordinates. This

has the potential to be a future research topic with implications to an increased understanding of tropical mountainous islands and their effects on surrounding atmospheric variables. Additionally, the change in temperature between 1000hPa and 510hPa do not vary much between the model scenarios over the open ocean. The largest variations are between CCSM3 PI of 29.5°C and CCSM4 LGM of 32°C, which further indicates the CCSM4 LGM run has a steeper lapse rate than all other model runs. The steeper lapse rate is consistent with the results from the aforementioned dry air entrainment radiative-convective model. However, this difference is not significant and only varies by 2.5°C from the smallest and largest surface-to-500hPa temperature decrease.

In order to analyze the precipitation rate across the WPWP, one must first distinguish between the convective precipitation rate (precc) and the large-scale (stable) precipitation rate (precl). CCSM4 LGM runs only output the total precipitation rate making the results based on analyzing the total precipitation rate as opposed to a distinction between the convective or large-scale precipitation rates, but the WPWP mostly undergoes convective precipitation as will be evident in the following discussion and therefore the emphasis of this section. Table 3.3 shows total precipitation rates by category. It is clear, and observed, that convective clouds produce the vast majority of precipitation in the WPWP, however, during the LGM period the models predict the convective precipitation takes an even larger role as the large-scale rate falls according to CCSM3. For CCSM4, all that can be stated is the amount of precipitation in the WPWP is much less (0.139 mm/day) during the LGM than the PI period. From Figure 5.22, CCSM3 output shows large increases of precipitation during the LGM along the equator in the western Pacific of up to 2 mm/day and large decreases

	CCSM3			CCSM4		
Variable	LGM	PI	LGM-PI	LGM	PI	LGM-PI
PRECC	6.3	5.9	0.4	—	5.3	—
PRECL	0.2	0.9	-0.7	—	1.8	—
TOTAL	6.5	6.8	-0.3	6.9	7.1	-0.2

Table 3.3: Individual variable and total precipitation rates (mm/day) for the WPWP. PRECC is the convective precipitation rate and PRECL is the large-scale (stable) precipitation rate.

in the southern portion of PNG and north of 9°N which is likely a result of the increased rising vertical motion near the equator. CCSM4 represents more zonal bands of increases and decreases in the precipitation rate, specifically a large decrease of more than -3 mm/day over all of PNG and an increase greater than 1 mm/day along the equator. Overall, the modeled LGM period sees 0.33 mm/day and 1.32 mm/day less precipitation in CCSM3 and CCSM4, respectively. Thus indicating agreement that the LGM period was a time of less precipitation in the WPWP, but not agreement in magnitude change.

The changes in evaporation rates from the LGM to PI across the WPWP were very small in both CCSM3 and CCSM4, where the models simulate a 0.2 mm/day increase and 0.3 mm/day increase over the entire region, respectively. This would be expected as CCSM3 shows a decrease in large-scale precipitation therefore decreasing the amount of cloud cover over the region. Figure 5.23 shows the large area of evaporation rate increases (less than 0.5 mm/day) in CCSM3 are almost balanced by the smaller area of large evaporation rate decreases (up to -3 mm/day) over the Sahul Shelf region. The latter is represented in CCSM4; however, the large positive evaporation rate differences do not exist near the equator as much as in CCSM3. The Sahul Shelf is represented in CCSM4 by a

much larger area of evaporation rate decreases compared to CCSM3, which is a direct response to the different model grid resolutions and higher topography in CCSM4.

The changes in surface wind speed and direction can be broken down into zonal and meridional directions for ease in understanding the separate components. For CCSM3 across the WPWP during LGM, the zonal wind was stronger easterly by 0.8 m/s and the meridional wind was weaker northerly by 0.3 m/s. For CCSM4, the zonal wind was stronger easterly by 1.3 m/s, however, was stronger southerly by 0.3 m/s. Therefore the change in zonal wind was in agreement between the two models, but the change in meridional wind was not. Specific features from CCSM3 surface winds during LGM (Figure 5.24) include a decrease in the transport from northern Australia to western PNG over the Sahul Shelf and a decrease in the easterly trade winds. This decrease in trade winds would have caused a decrease in equatorial upwelling resulting in a smaller temperature difference near the equator when compared to the corresponding areas around the equator. Features of CCSM4 LGM surface winds include weaker transport across the Sahul Shelf region than CCSM3 as a result of the increase in topography resolved within CCSM4. Features from CCSM3 minus CCSM4 surface wind show a decrease in Northern Hemisphere subtropical transport and easterly trade winds in CCSM4 during both the PI and LGM runs. This indicates less subtropical dry air intruding into the WPWP, which would have kept the surface relative humidity of the LGM similar to what it is presently. The extended region surface wind pattern shows the increased NH subtropical air flowing directly into the WPWP in CCSM3 and little to no changes in the transport for CCSM4 from the LGM to PI runs which further indicates that the CCSM3 model run transported

	CCSM3			CCSM4		
Wind Direction	LGM	PI	LGM-PI	LGM	PI	LGM-PI
U (m/s)	-6.4	-5.2	-1.2	-6.5	-6.1	-0.4
V (m/s)	0.1	1.1	-1.0	-0.7	0.1	-0.8

Table 3.4: WPWP area average wind (m/s) in the zonal (U) and meridional (V) directions at 510hPa. Negative values correspond to easterly wind in the U-direction (zonal) and northerly wind in the V-direction (meridional).

drier air into the WPWP compared to the CCSM4 run. This would affect the surface relative humidity to decrease and atmospheric lapse rate to increase in CCSM3 runs, which was discussed earlier.

The average zonal wind at the 510hPa level increased in magnitude in the easterly direction during the LGM by 1.2 m/s for CCSM3 and 0.4 m/s for CCSM4. The WPWP-averaged meridional wind is southerly for all model runs except CCSM4 LGM, however, as seen in Table 3.4 each model change from LGM to PI shows increases in the northern wind values representing an increase in transport to the north averaged over the WPWP or in other terms the LGM was a time when northern transport was not as strong compared to PI runs. The average meridional wind decreased similarly in both models with 1.0 m/s for CCSM3 and 0.9 m/s for CCSM4. Specific features from the CCSM3 510hPa wind include large increases in LGM easterlies north of the equator and an increase in equatorial transport around PNG and Australia. The most striking feature from CCSM4 is that the LGM zonal wind north of the equator is faster east of 142°E and slower west of 142°E compared to the PI run. This may be caused by a decrease in wind speeds as they approach Southeast Asia and higher topography due to decreases in sea level. The predominant difference between the two models is the increase in 510hPa level equatorial winds in CCSM4 for both the LGM and PI runs and

a stronger upper-level subtropical high pressure in CCSM3 north of the WPWP in the LGM runs.

The surface WPWP streamlines (Figure 5.25) for the CCSM3 PI run has more direct transport from the northern hemisphere subtropics as the tracer placed at 15°N, 165°E travels across the WPWP to ∼3°N, 130°E whereas the same tracer for the CCSM4 PI run only goes as far south as ∼9°N. This indicates CCSM3 has a tendency to transport drier subtropical air into the WPWP whereas CCSM4 keeps most of the subtropical transport north of 6°N and away from the center of the WPWP. Evidence for this can be seen in the precipitation rate analysis above as CCSM3 PI has ∼1.6 mm/day less than CCSM4 PI. This continued for the LGM runs albeit not to as extreme meridional distances where the same tracer for CCSM3 transported subtropical air slightly north of 6°N and the CCSM4 LGM run to ∼10.5°N. This indicates that the cooler WPWP during the LGM may have had a higher relative humidity than present-day as a result of a reduction in the Northern Hemisphere dry-air advection into this region The equatorial transport for each model showed roughly the same result with a parcel starting at the equator travelling to the region of western PNG. The only exception is CCSM3 PI has the tracer travelling north of PNG and drifting out of the WPWP region at the equator instead of into PNG. It is clear from a comparison of CCSM3 and CCSM4 above PNG that the CCSM4 runs have a good depiction of the topography as the streamlines converge in the middle of the island and stop representing orographic lift whereas the CCSM3 run streamlines go through the island indicating a lack of high enough mountainous terrain representation. The southeastern WPWP streamline tracer (15°S, 165°E) transports subtropical air directly into PNG for each model indicating there is no change from PI to LGM

conditions therefore not influencing the amount of dry/moist air transport into the WPWP. The final WPWP surface streamline analysis is over the Arafura Sea/Sahul Shelf region from an initial point of 15°S, 150°E. The CCSM3 PI run streamline transports a parcel south of PNG all the way to the equator and represents the farthest point north of all model run transports for this specific tracer. The other model runs show transport south of PNG and a more zonal route to ∼9°S. However, as the majority of streamlines south of the equator and east of PNG have direct transports into the center of the WPWP, it is not expected that the small deviations in the Arafura Sea/Sahul Shelf region would impact the amount of dry air transport to change the precipitation rate. Therefore, the largest difference between the model streamlines is the transport from the subtropical region of the Northern Hemisphere where CCSM3 tends to bring drier surface air into the WPWP whereas CCSM4 tends to keep the drier air farther north of the central WPWP. Furthermore, both CCSM versions have less Northern Hemisphere subtropical, dry-air advection into the WPWP potentially maintaining, if not increasing, the surface relative humidity at present-day values in this region during the LGM.

Figure 5.26 represents the extended region surface streamlines in order to obtain a better understanding of surface transport into the WPWP. The extended region surface streamline tracer beginning at 20°S, 140°W does not show a large difference between the four model runs. However, the tracer commencing at 20°N, 140°W does differ between the models where CCSM3 tends to transport the parcel farther south into the WPWP, just north of the equator, and CCSM4 keeps the parcel at a trajectory farther north from the WPWP for the PI and LGM runs. This is in agreement with the aforementioned surface streamline analysis further

indicating that the CCSM3 model tends to transport drier surface air into the WPWP region while CCSM4 does transport it into the WPWP but not as direct or deep into the center of the WPWP. This supports the idea that CCSM4 runs will have a more moisture in the WPWP leading to larger precipitation rates as suggested in the precipitation analysis.

Further up in the atmosphere, the 510hPa WPWP streamlines are mainly zonal for each of the different model runs. The CCSM4 runs tend to be more zonal across the entire WPWP, whereas the CCSM3 runs are zonal in structure but have smaller scale troughs and ridges in both the PI and LGM runs. Subtropical dry air transport at 510hPa does not change between the models resulting in no noticeable large-scale changes in atmospheric transport during the LGM. The same can be said for the extended region 510hPa streamline analysis. Therefore the most important changes in LGM dry air transport reside in the surface transport from the Northern Hemisphere.

CHAPTER 4

Conclusion

From this research, the moist-adiabatic lapse rate for the highly convective WPWP is not the best approach for understanding the vertical structure of the present-day or LGM period in the western Pacific warm pool [61]. Analysis of the DOE ARMS datasets for Nauru and Manus showed the mean vertical structure of the troposphere cannot be described by a moist adiabat. The WPWP has an annual-average surface temperature of 28.8°C and the height of the freezing level averages 5200m according to sounding data. Applying the moist adiabatic approach to present-day WPWP conditions results in a freezing level of 6000m above the surface or 800m above sounding data and 1300m above the glacial extent. As a result, the moist adiabatic approach in the WPWP is not an appropriate technique for calculating atmospheric freezing levels in the tropics [61].

Use of an entraining model to simulate modern and LGM mean vertical structure shows this model can reproduce observations by entraining lower relative humidity free-tropospheric air into an ascending parcel. Absolute freezing levels for the LGM are 4900m assuming SSTs of 25.3°C (3.5°C SST reduction) with a non-entraining model, and 3620m with an entraining model. The model sensitivity results stated changing the surface temperature 1°C decreased the freezing level 235m, reducing the surface relative humidity 1% decreased the freezing level 40m,

and a 1% reduction of free tropospheric relative humidity decreased the freezing level 25m [61]. Therefore, the WPWP during the LGM was ∼3.5°C cooler than the pre-industrial era based on the entraining model and the glacial extent levels. These sensitivities and present-day WPWP conditions were able to replicate the vertical structure in the entraining model whereas the moist adiabatic approach was not able to replicate this structure. Therefore, entrainment plays a vital role in WPWP dynamic processes and should be included in all models in the future.

By analyzing two model versions (3 and 4) of the Community Climate System Model, it is evident that in a GCM, the effects of entrainment on the vertical temperature structure in the WPWP are important. Since the WPWP is an area of active convection year round, the differences in the vertical temperature structure of CCSM3 and CCSM4 did result in larger lapse rates for CCSM4 where the entrainment scheme was updated to more realistically represent atmospheric convection. The CCSM runs both output surface temperature changes during the LGM that are much smaller than the recently published Mg/Ca or clumped isotope paleothermometry data. However, the updated version of the model has a much better handle on WPWP processes like precipitation rate due to the enhanced grid resolution and the updated entrainment scheme. The CCSM runs (both PI and LGM) indicate that although the model is not perfect, as was expected, but is improving significantly over time.

An important model component taken from this paper is that transport of drier subtropical surface air from the Northern Hemisphere was not as large during the LGM compared to the PI runs. This indicates that even though the LGM was a period of colder temperatures and less convective activity (reduced precipitation rates), if the LGM period was a time of reduced dry-air advection from

the Northern Hemisphere subtropical regions into the WPWP this would have resulted in decreased subtropical-tropical air mass mixing causing the surface relative humidity to be similar or even larger than present-day values, during the LGM. Therefore, a lower surface temperature combined with small changes in the atmospheric moisture would preserve the surface relative humidity resulting in no large differences from present-day to LGM surface relative humidity values.

The model runs have previously known biases and flaws, however this thesis has pointed several key issues. The most significant is the mountain boundary layer, discrepancy between temperature over the mountain and open ocean that was evident all the way up to the upper-levels of the troposphere. If this is persistent above all mountain ranges, then it represents a significant flaw in the model versions and should be looked at for future work.

Much more work needs to be done in the area of paleoclimate modeling. It is important to understand that if the scientific community has a handle and comprehension of extreme climates of the past, they can begin to predict what will happen in the future to a greater degree of confidence.

CHAPTER 5

Figures

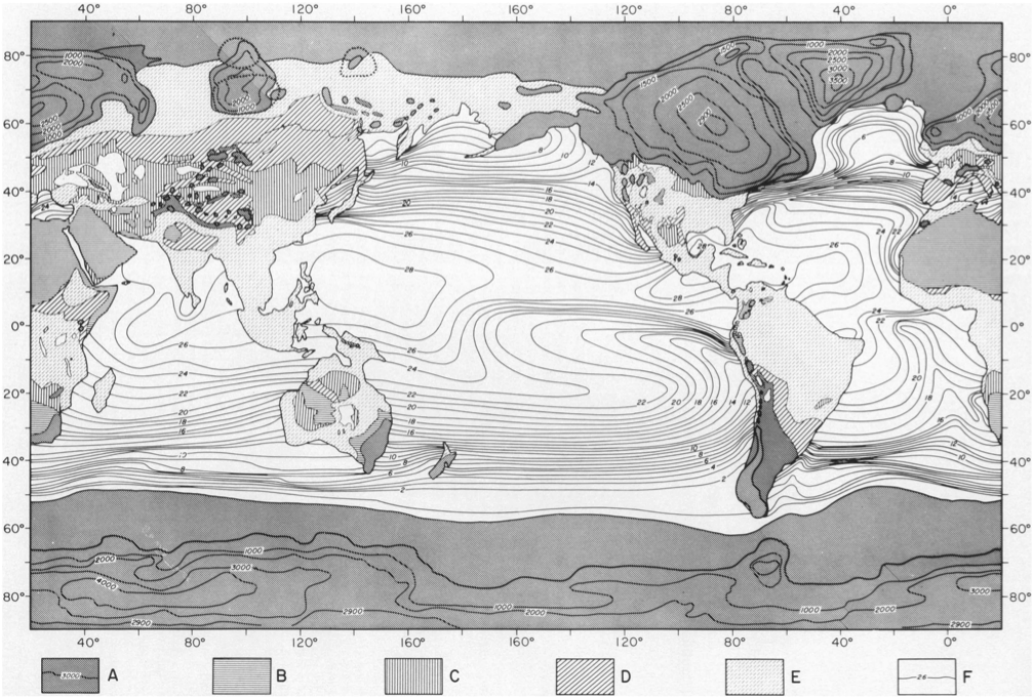

Figure 5.1: From *CLIMAP Project Members* (1976), SST, ice extent, ice elevation, and continental albedo for Northern Hemisphere summer (August) 18,000 years ago. CLIMAP found warm pool cooling of ∼1°C during the LGM. Contour intervals are 1°C for isotherms and 500m for ice elevation. Continental outlines a sea level lowering of 85m (believed sea level lowering at the time). Albedo values are given by the key. (A) Snow and ice; albedo over 40%. Isolines show elevation of the ice sheet above sea level in meters. (B) Sandy deserts, patchy snow, and snow covered dense coniferous forests; albedo between 30-39%. (C) Loess, steppes, and semideserts; albedo between 25-29%. (D) Savannas and dry grasslands; albedo between 20-24%. (E) Forested and thickly vegetated land; albedo below 20%. (F) Ice-free ocean and lakes, with isolines of SSTs in °C; albedo below 10%.

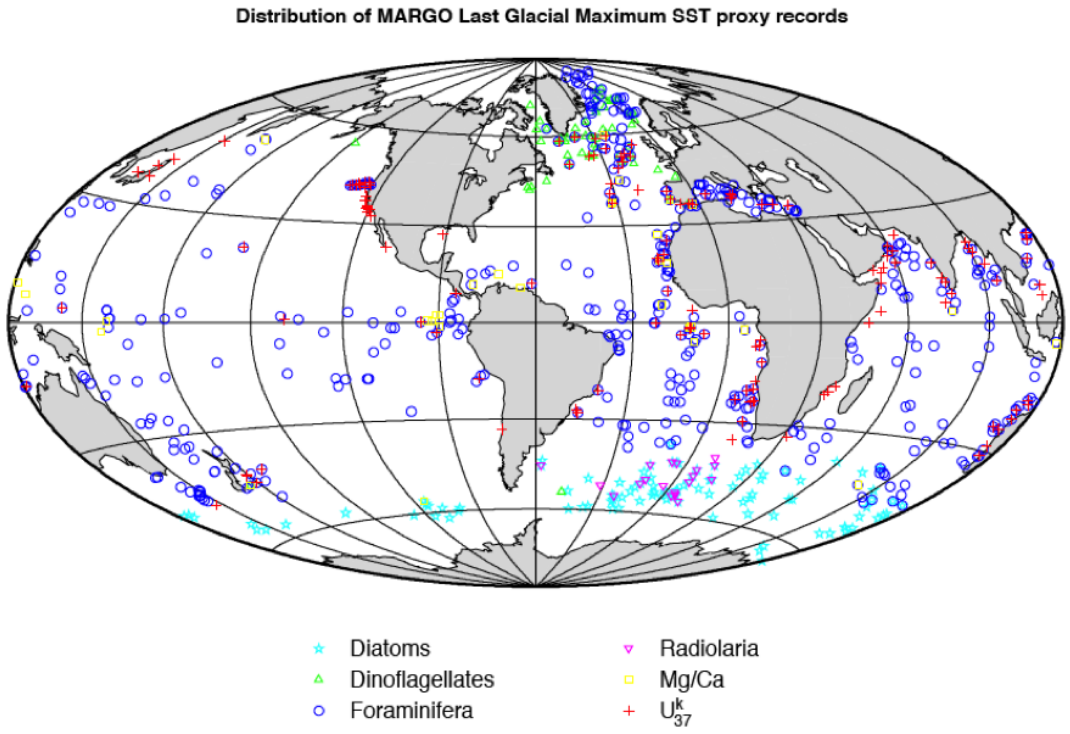

Figure 5.2: Location of proxy records of LGM SST included in the MARGO reconstructions [30].

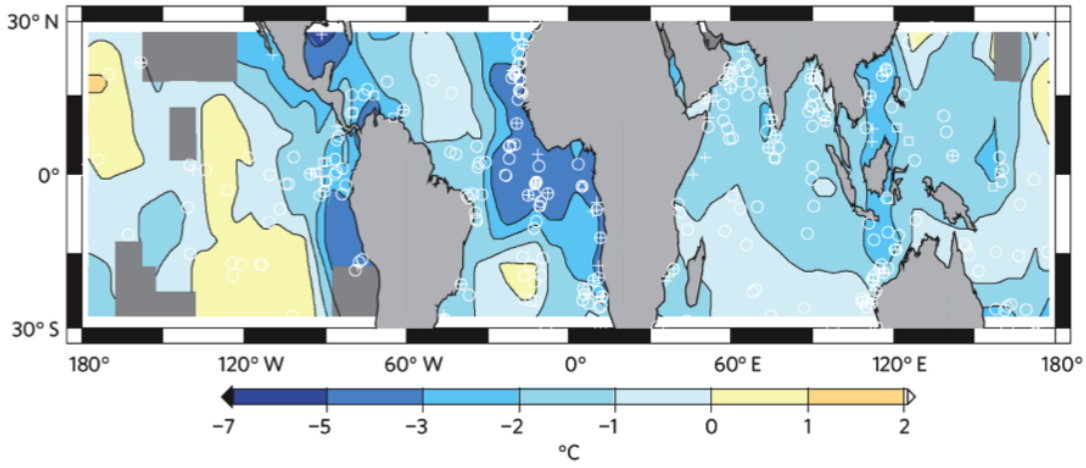

Figure 5.3: Map of reconstructed LGM annual mean temperature anomalies for the 30°S-30°N tropical band computed as LGM-World Ocean Atlas 1998 [34].

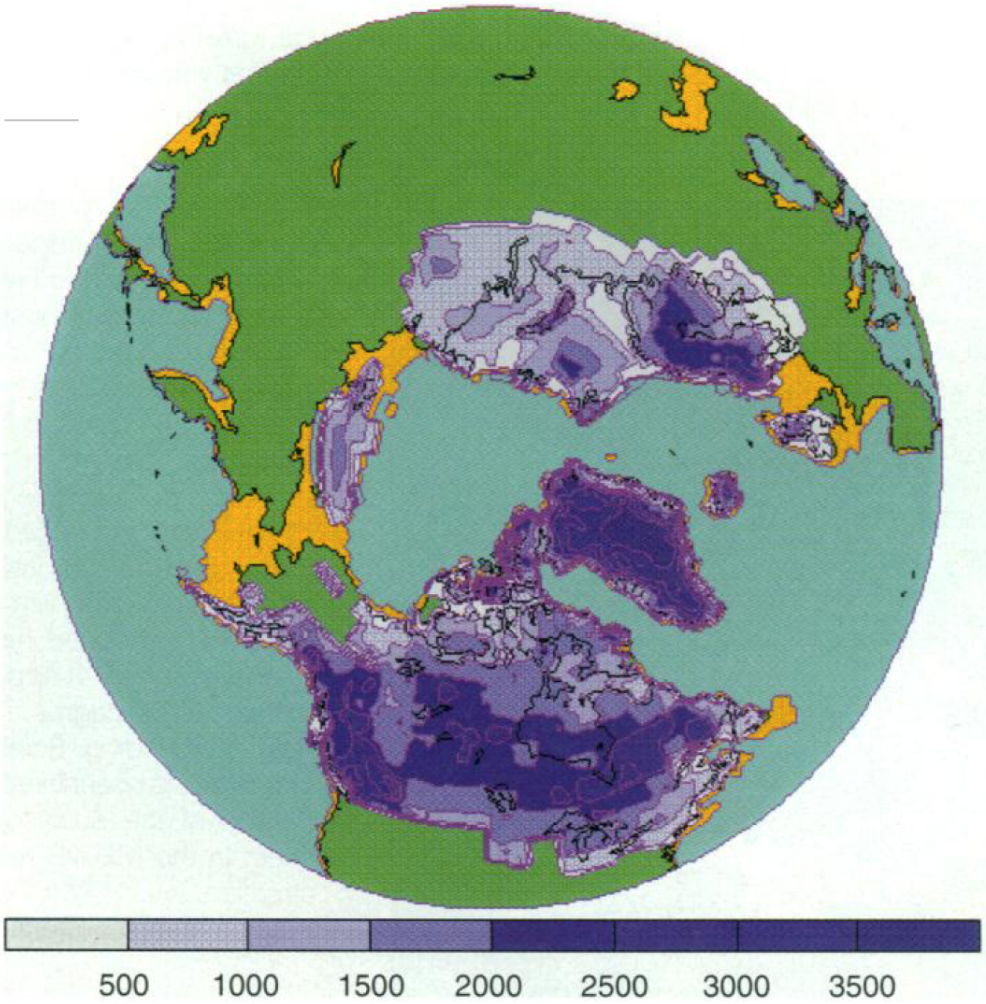

Figure 5.4: LGM ice sheet boundary conditions for PMIP where the height is in meters relative to sea level [42].

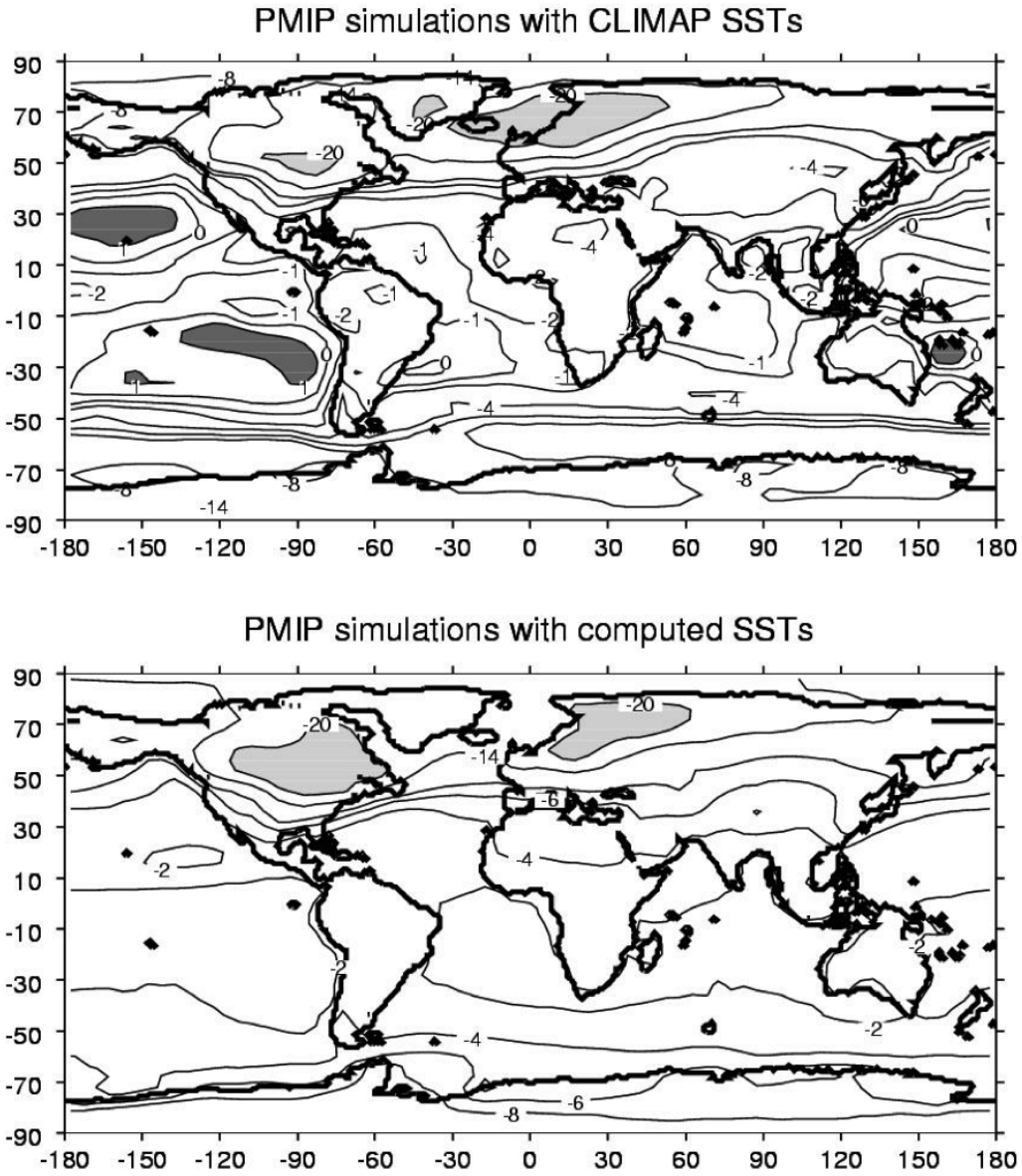

Figure 5.5: Annual mean changes in surface air temperature at the LGM. Average of all the PMIP simulations interpolated to the same grid: (top) the 7 simulations using CLIMAP SSTs and (bottom) the 8 simulations using computed SSTs. Fields represent the LGM present-day values. Isolines at -20°C, -14°C, -8°C, -6°C, -4°C, -2°C, -1°C, 0°C, 1°C. Dark grey above 1°C and light grey below -20°C [27].

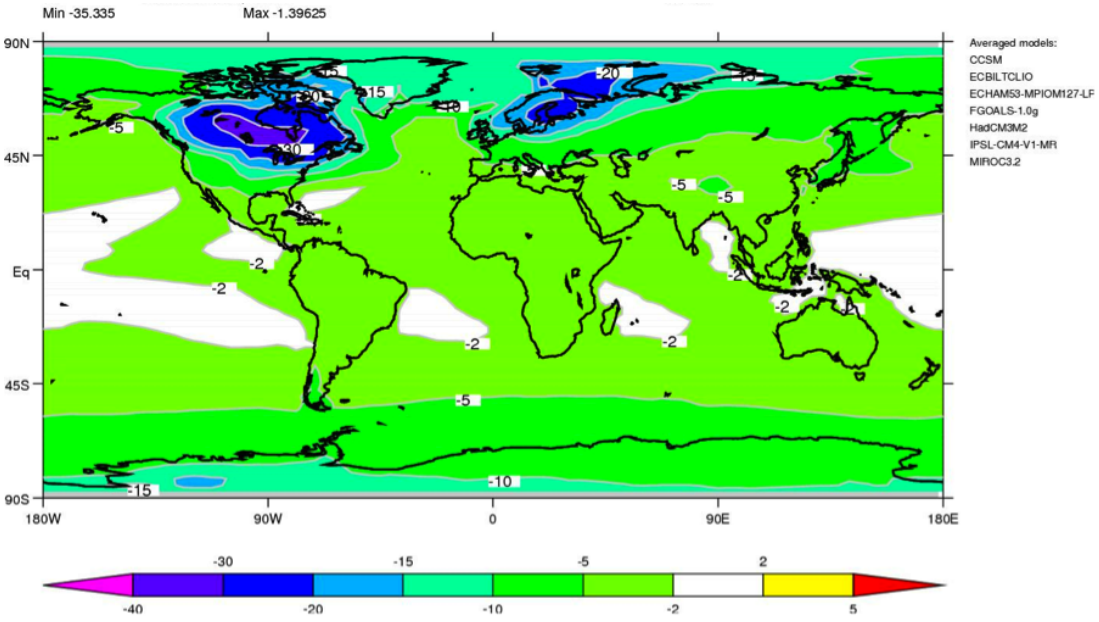

Figure 5.6: Model average surface air temperature change (LGM-0k) in °C from the PMIP2 LGM database.

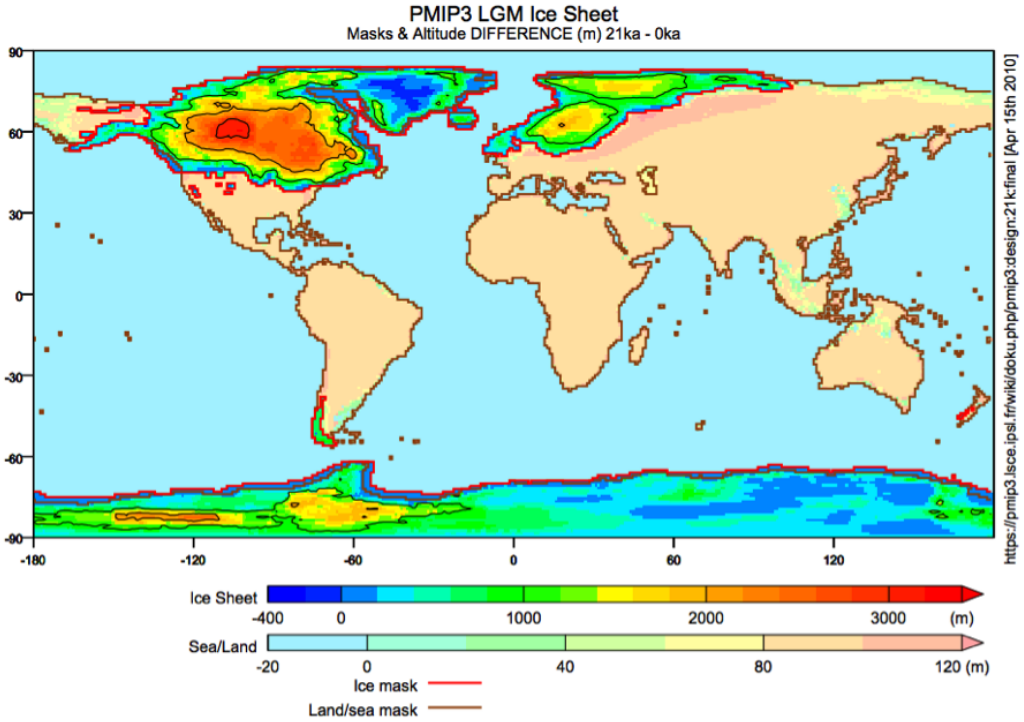

Figure 5.7: PMIP3 LGM boundary condition for ice sheet extent and height (in meters) from the PMIP3 dataset.

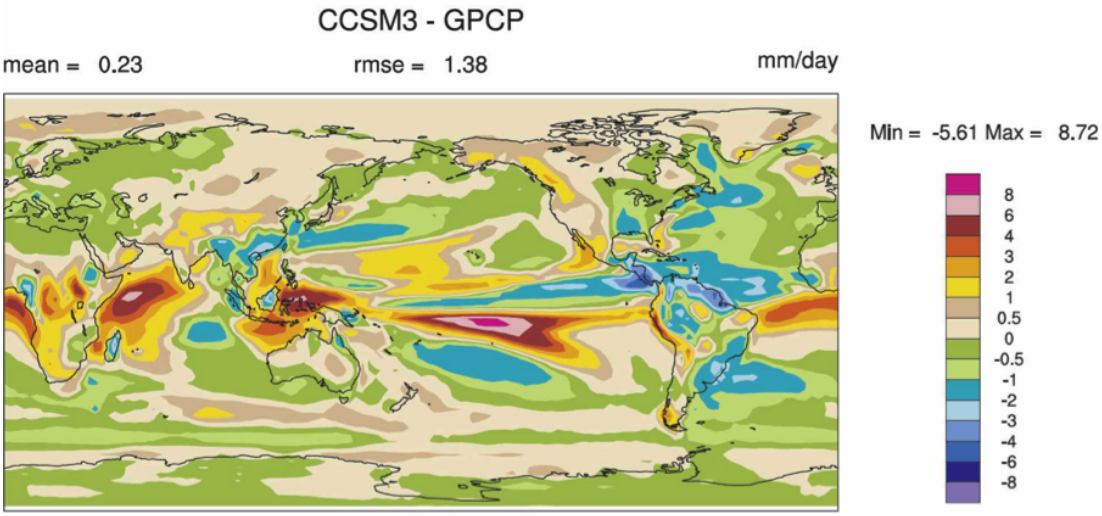

Figure 5.8: Differences in annual-mean total surface precipitation between the GPCP dataset and CCSM3 indicating model biases [11].

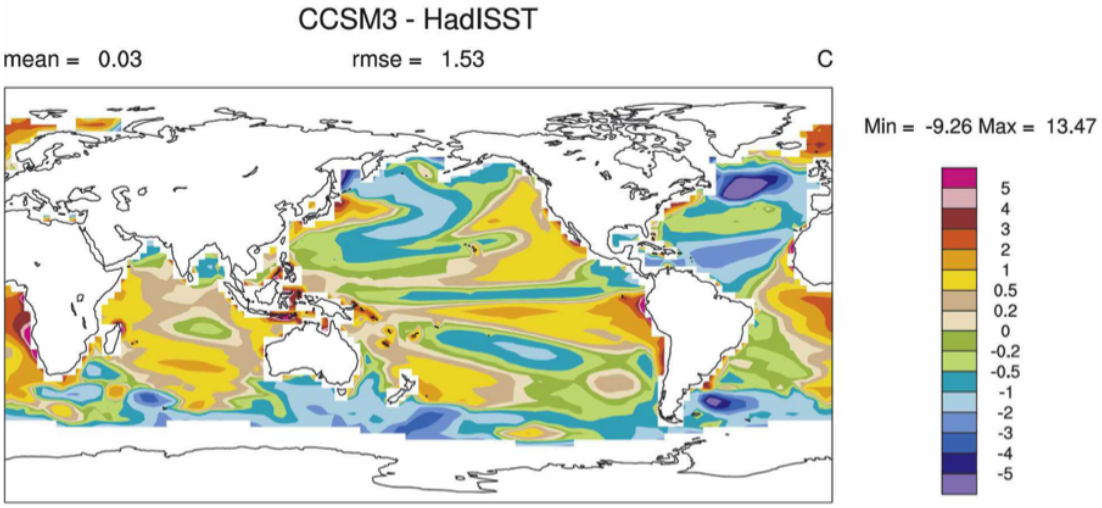

Figure 5.9: Differences in annual-mean surface temperature between the HadISST dataset and CCSM3 indicating present-day model biases [11].

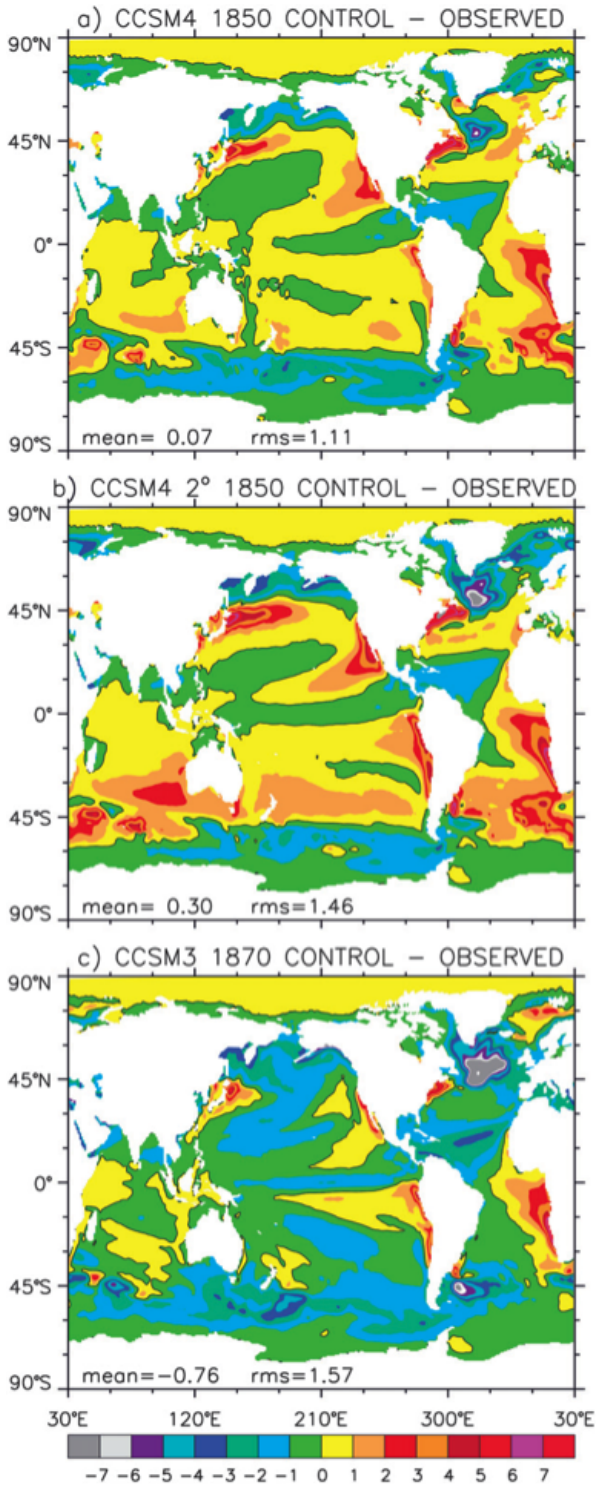

Figure 5.10: Mean SST (°C) from the *Hurrell et al.* (2008) observations. The observations use (1870-99) and all runs use (871-900) [18].

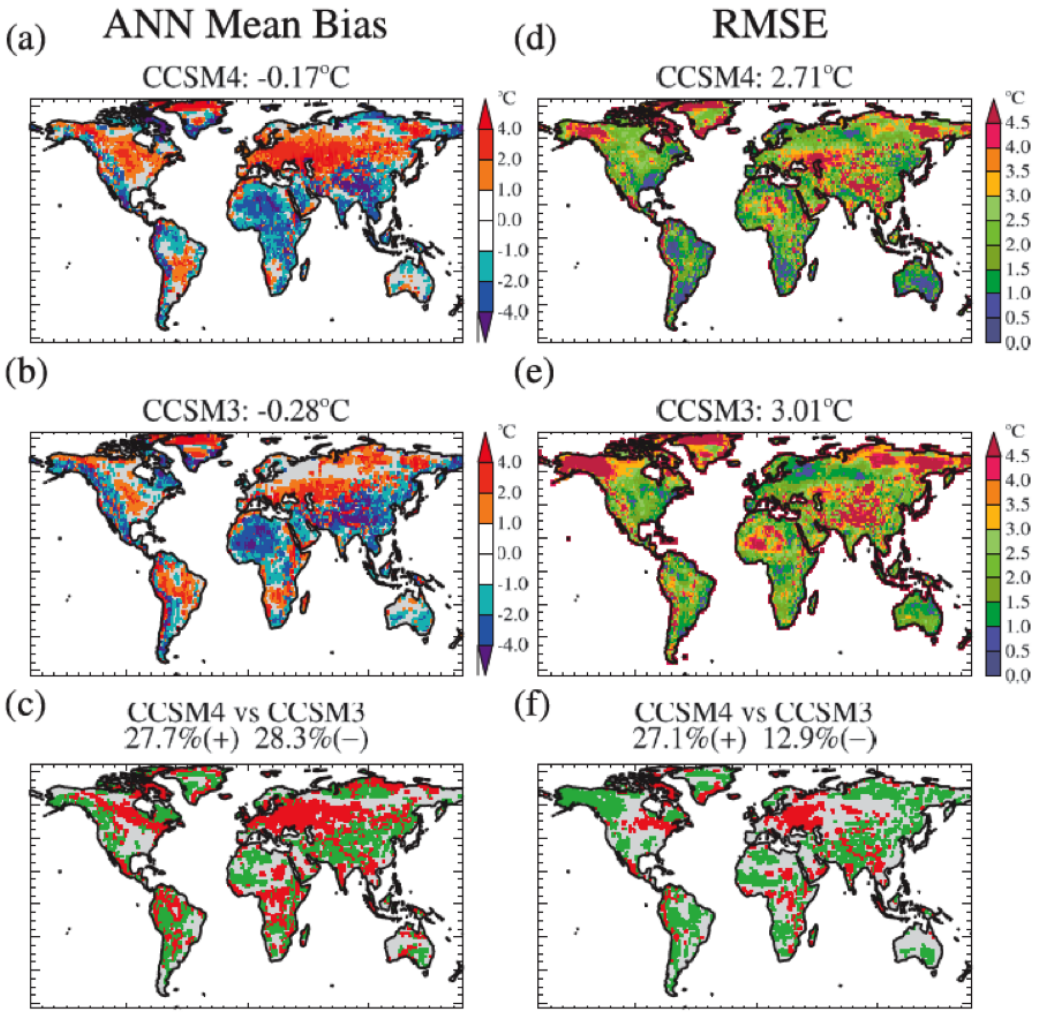

Figure 5.11: Differences of model land surface air temperature (°C) from observations from 1950-99. Models use the twentieth-century run. In (c) and (f) green (red) areas are where CCSM4 (CCSM3) is in better agreement with the observations; gray areas indicate no difference [18].

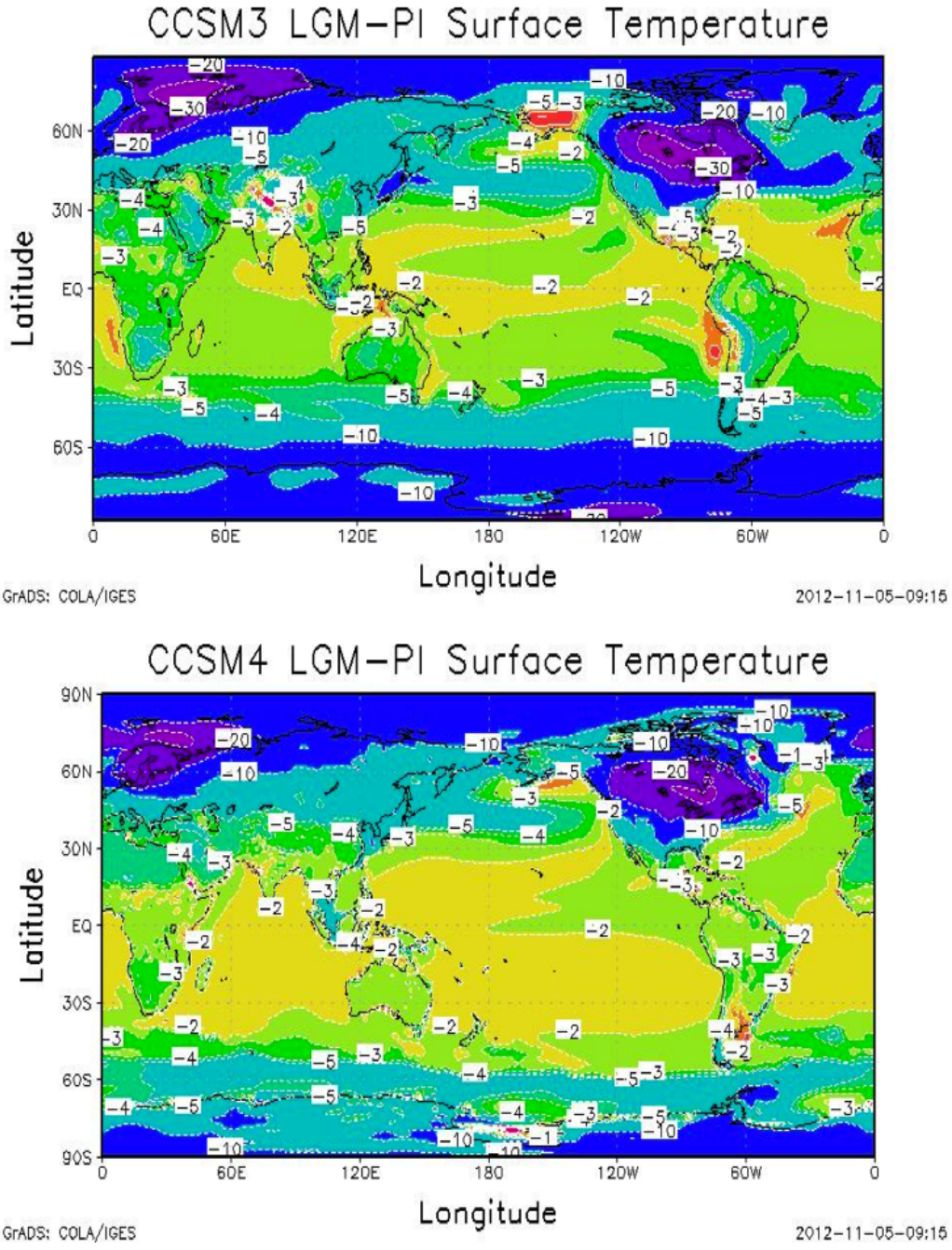

Figure 5.12: Annual mean change in surface skin temperature (°C) for CCSM3 (top) and CCSM4 (bottom) calculated as LGM-PI runs contoured at -30°C, -20°C, -10°C, -5°C, -4°C, -3°C, -2°C, -1°C, 0°C, and 1°C

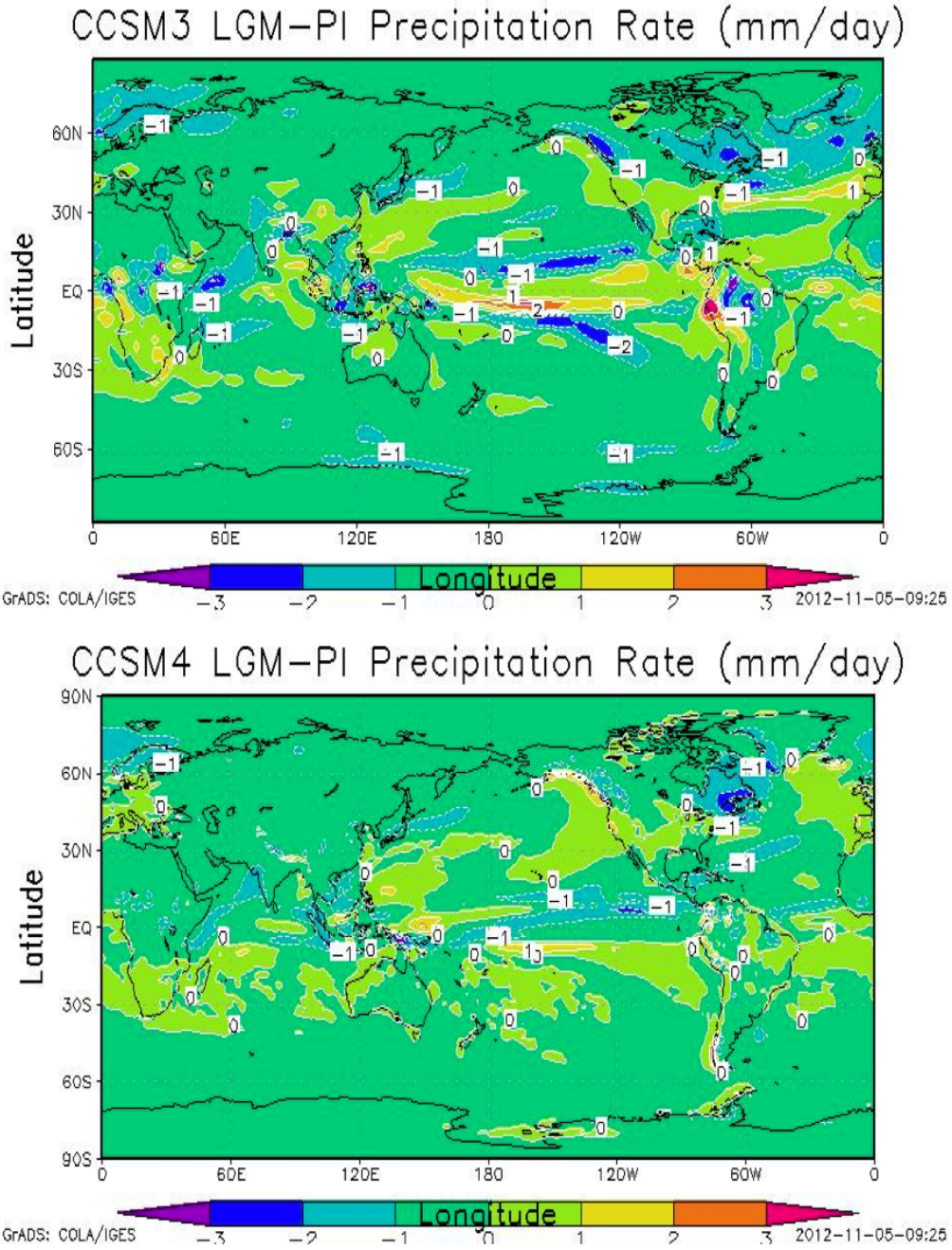

Figure 5.13: Annual mean change in precipitation rate (mm/day) for CCSM3 (top) and CCSM4 (bottom) calculated as LGM-PI runs countoured at -3, -2, -1, 0, 1, 2, and 3 mm/day.

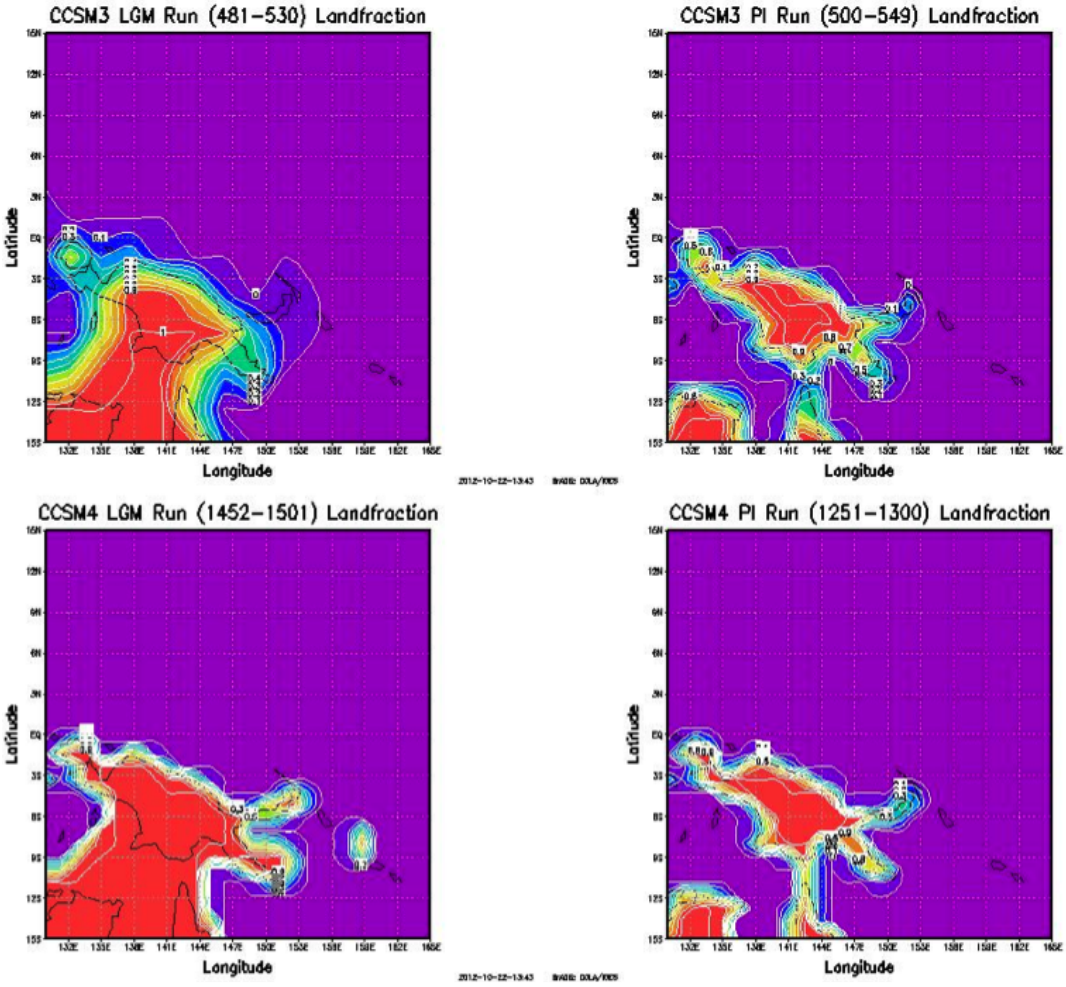

Figure 5.14: Fraction of land above sea level representing model topographic boundary conditions contoured at 0.1 increments where 1.0 is completely above sea level and 0.0 is below sea level.

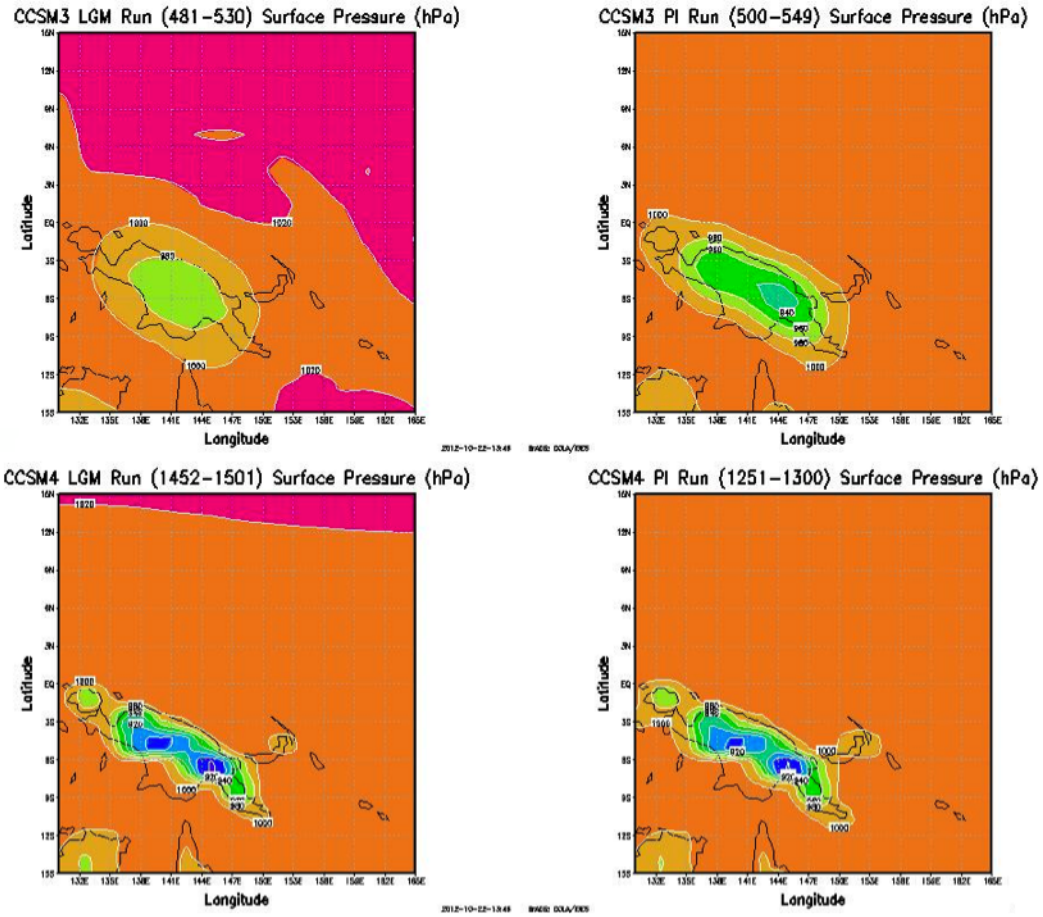

Figure 5.15: Annual mean surface pressure (in hPa) for the WPWP denotes the topographic increases due to higher resolutions in the CCSM4 model runs (bottom) compared to the lower resolution CCSM3 model runs (top). Contours are in 20hPa increments.

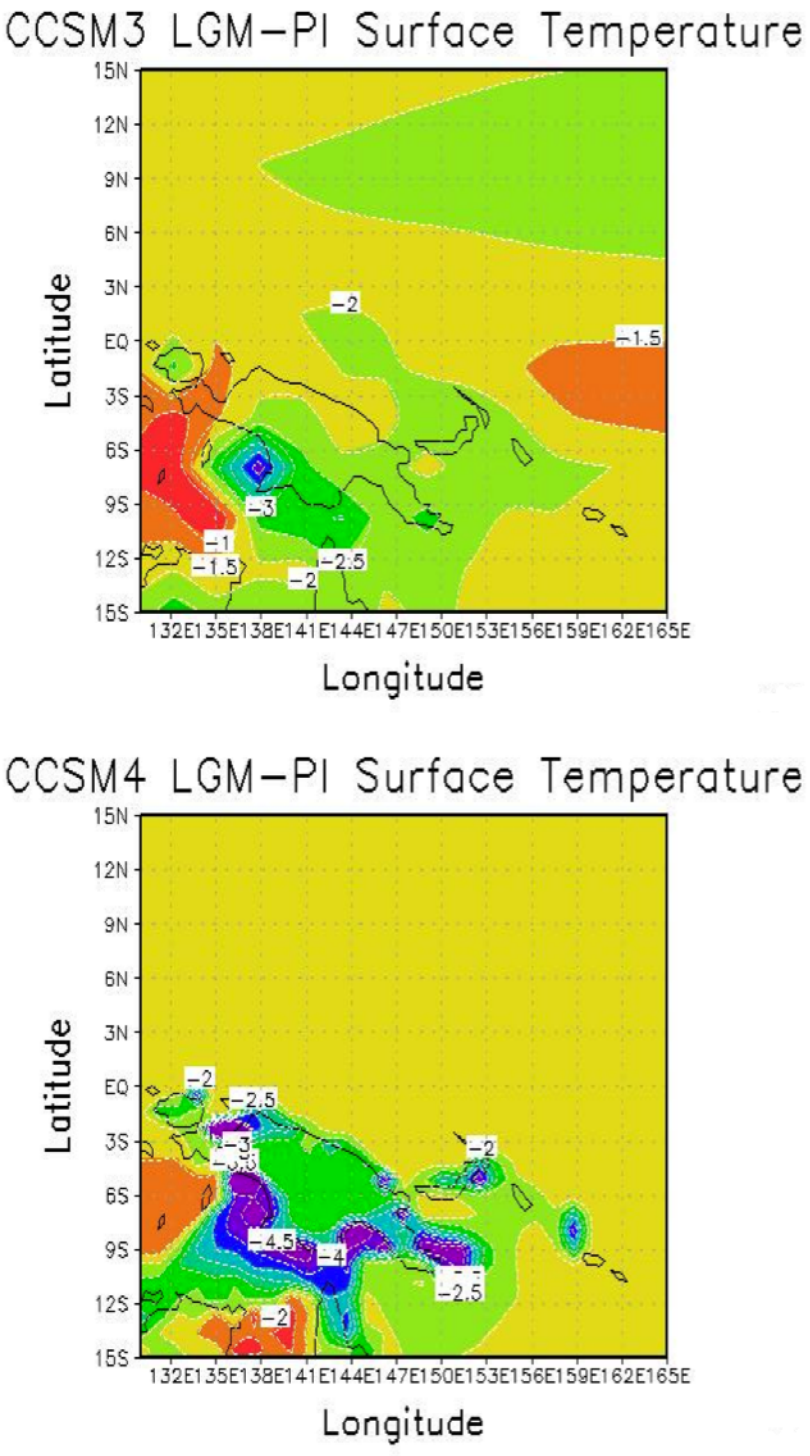

Figure 5.16: Annual mean change in surface skin temperature for CCSM3 (top) and CCSM4 (bottom) calculated as LGM-PI runs contoured at -5°C, -4.5°C, -4°C, -3.5°C, -3°C, -2.5°C, -2°C, -1.5°C, -1°C, and -0.5°C.

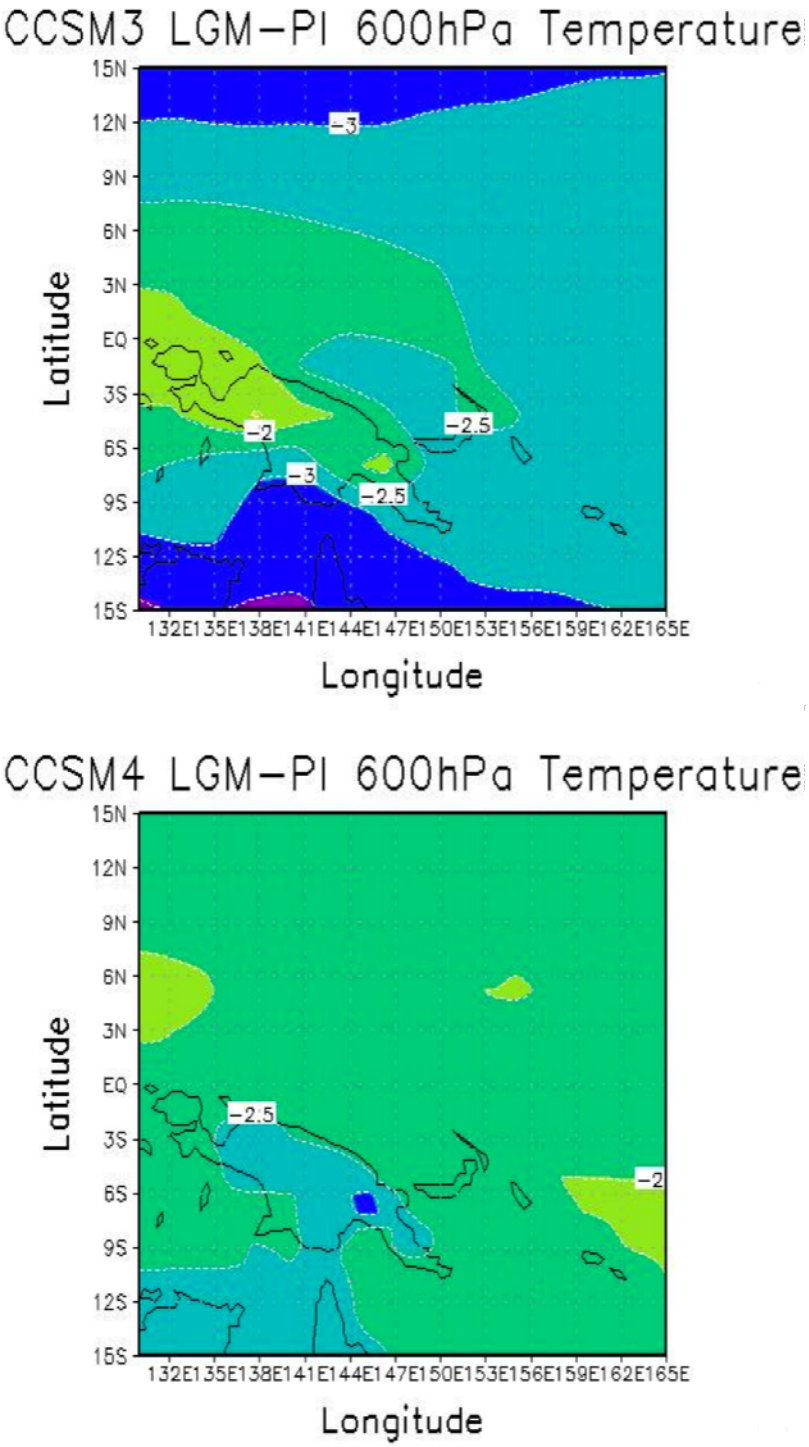

Figure 5.17: Annual mean change in 600hPa temperatures (°C) for CCSM3 (top) and CCSM4 (bottom) calculated as LGM-PI runs.

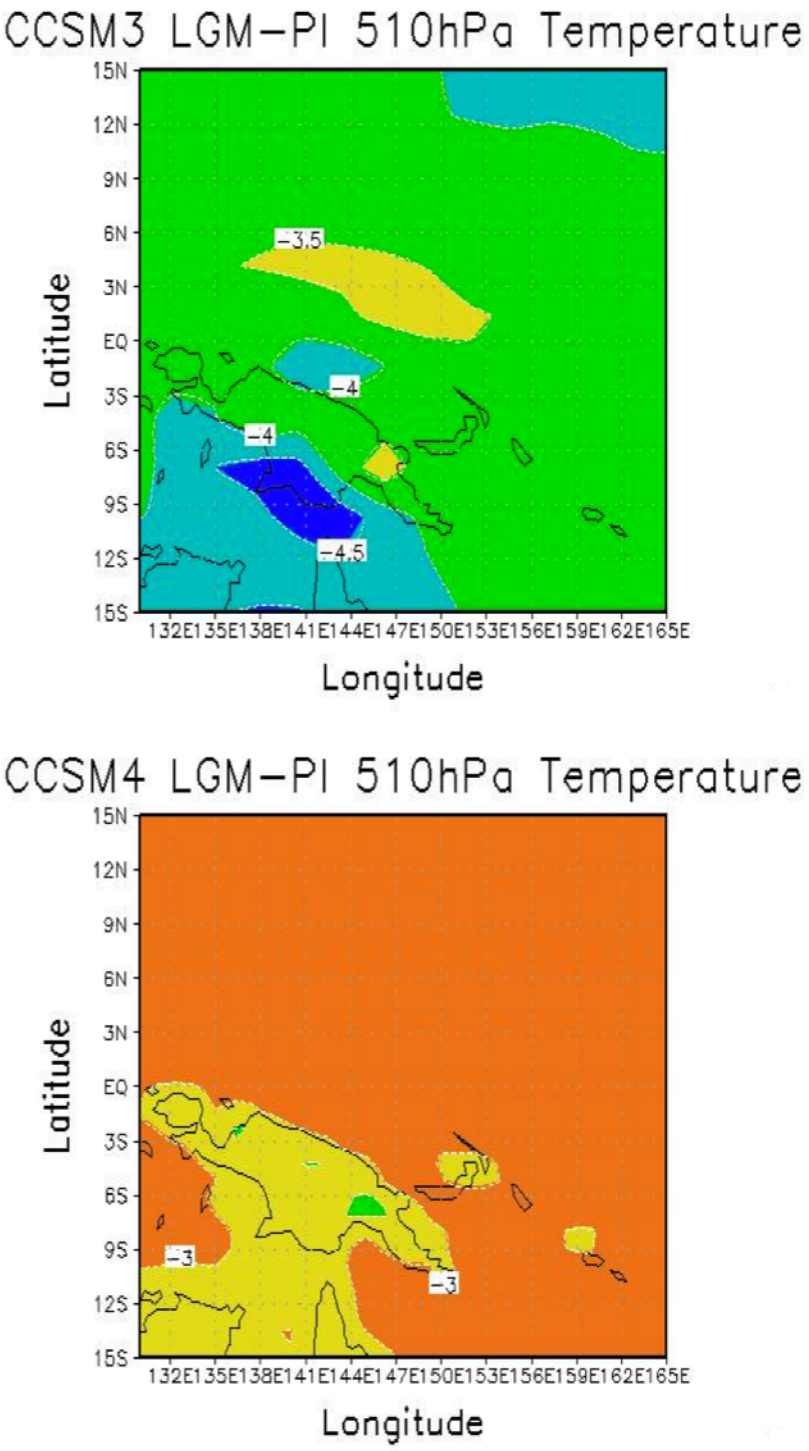

Figure 5.18: Annual mean change in 510hPa temperature (°C) for CCSM3 (top) and CCSM4 (bottom) calculated as LGM-PI runs.

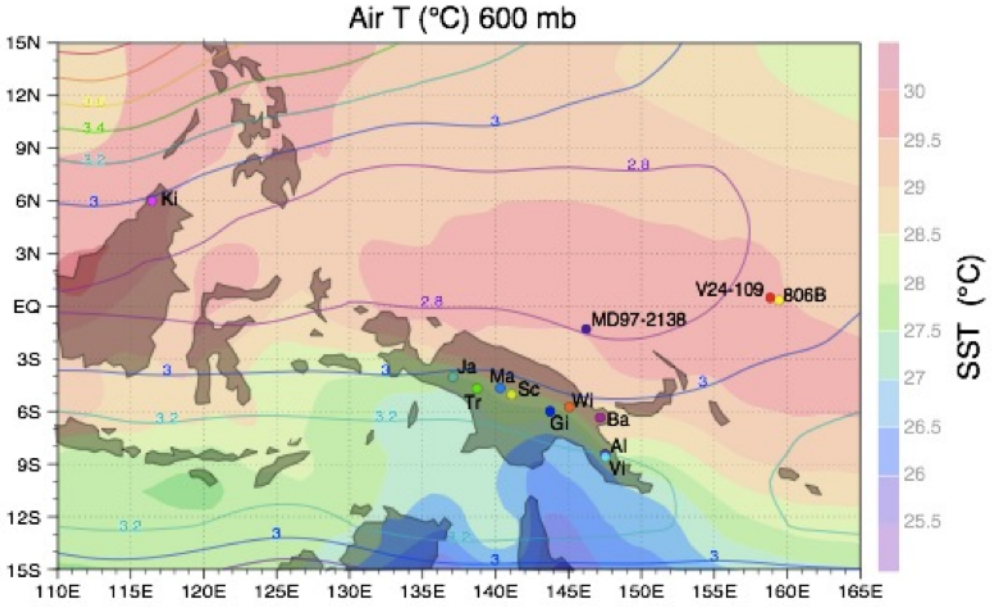

Figure 5.19: From *Tripati et al.,* (in review), sites studied and modern temperatures in the warm pool. Shown are core localities study (Ocean Drilling Program Site 806B, MD97-2138, and V24-109) and mountains in Papua New Guinea and Borneo that were glaciated at the LGM (Tr = Mount Trikora, Ki = Mt. Kinabalu, Gi = Mt. Giluwe, Wi = Mt. Wilhelm, Vi = Mt. Victoria, Ba = Mt. Bangeta, Ma = Mt. Mandala, Ja = Mt. Jaya, Sc = Mt. Scorpio, Al Mt. Albert Edward). Also shown are average summer (June-July-August) air temperatures at the 600hPa pressure level (for 1979-2010; NCEP2 re-analysis dataset) and SST (for 1982-2010; Reynolds re-analysis dataset). These datasets indicate that tropospheric temperatures over Papua New Guinea and Borneo typically is not more than a couple of tenths of a degree different from the same pressure level over the ocean, and that seasonal variability in average SST is typically less than 0.4°C at the three open ocean sites studied.

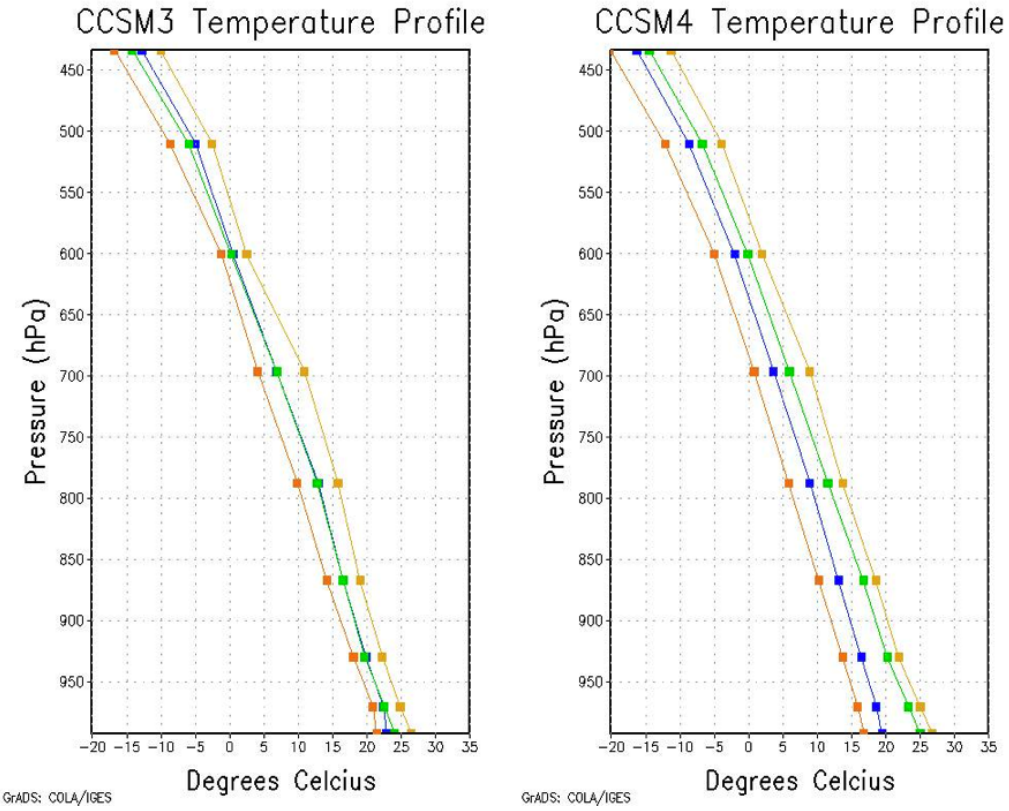

Figure 5.20: Annual mean vertical temperature (°C) profile above PNG (orange=LGM and blue=PI) and a paleothermometry location (green=LGM and yellow=PI). The freezing level heights for CCSM3 are 4345m at the LGM and 5031m for the PI run compared to 4247m at the LGM and 4731m at the PI run for CCSM4.

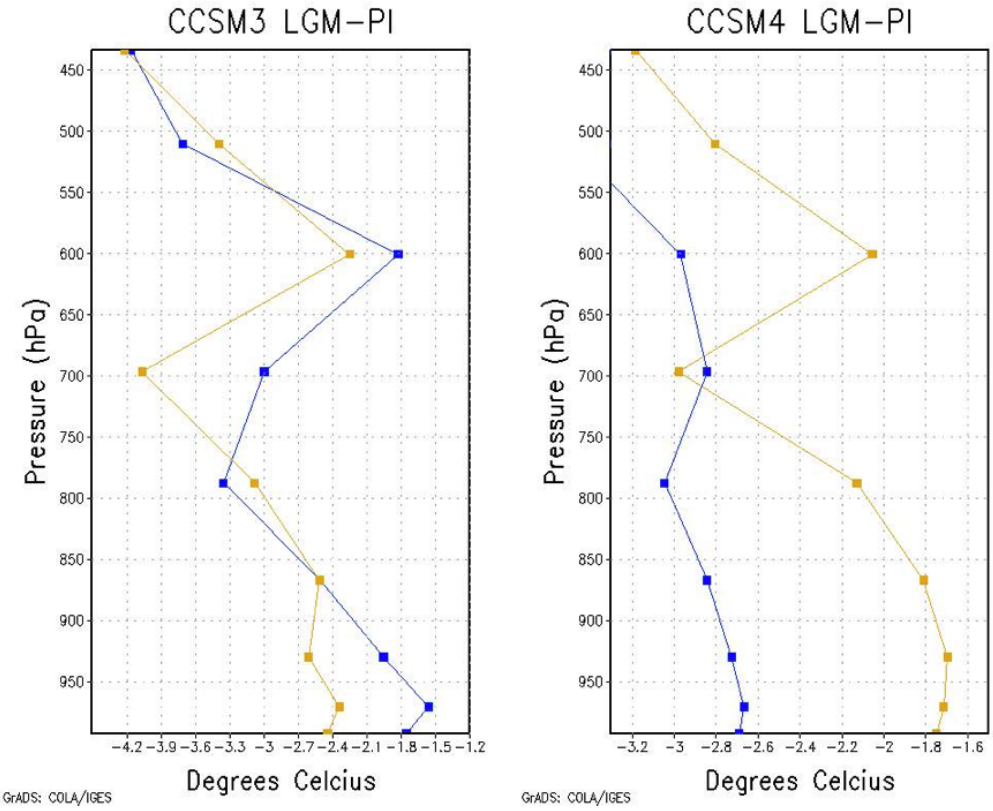

Figure 5.21: Annual mean vertical temperature (°C) profile change from LGM-PI control run. The blue line represents the location above PNG and the yellow line is above the paleothermometry location. The heights above sea level are 1000m at ∼900hPa, 2000m at ∼800hPa, 3000m at ∼710hPa, 4000m at ∼630hPa and 5000m at ∼560hPa.

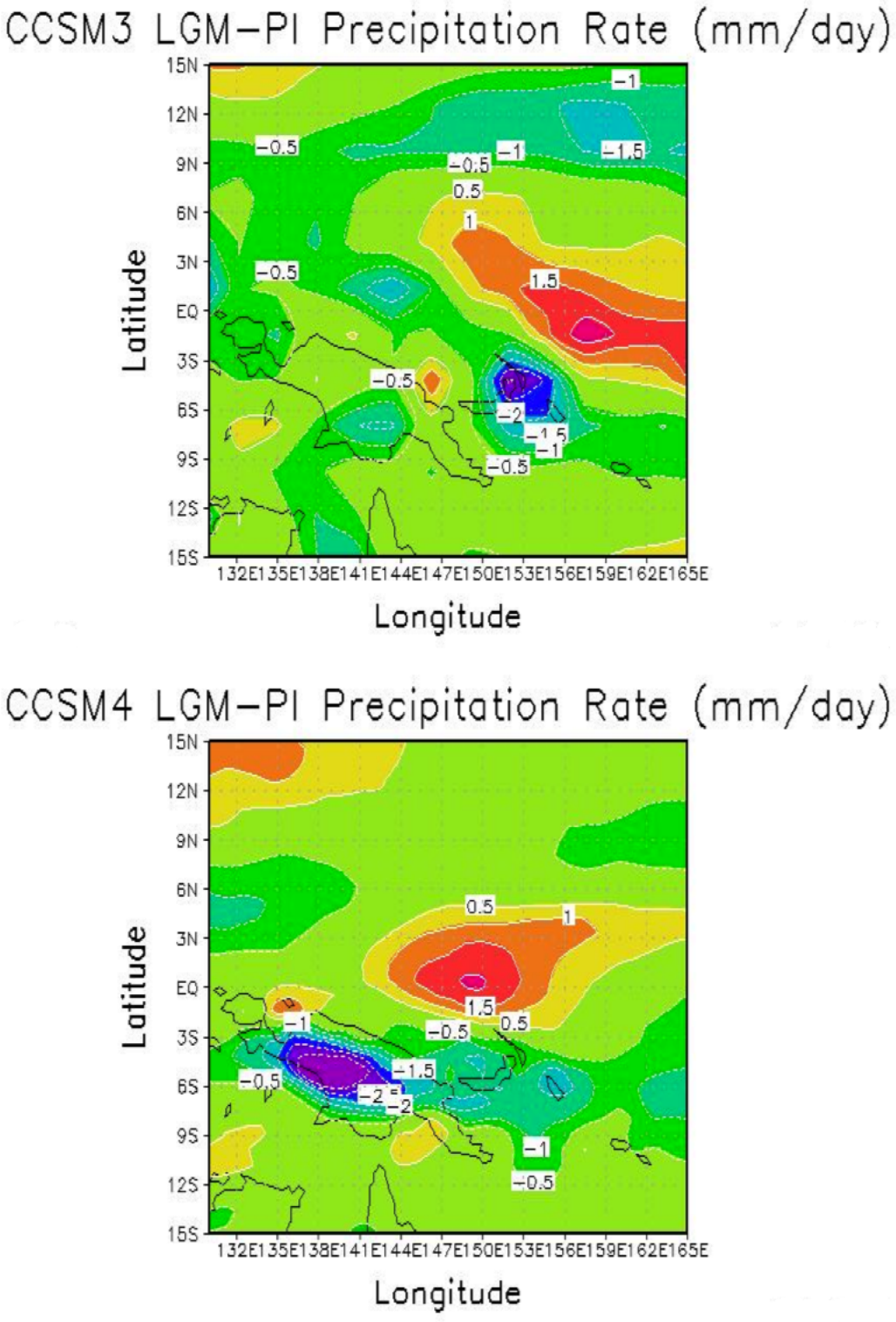

Figure 5.22: Annual mean change in total precipitation rate (mm/day) for CCSM3 (top) and CCSM4 (bottom) calculated as LGM-PI runs and contoured at -3, -2.5, -2, -1.5, -1, -0.5, 0.5, 1, 1.5, and 2 mm/day.

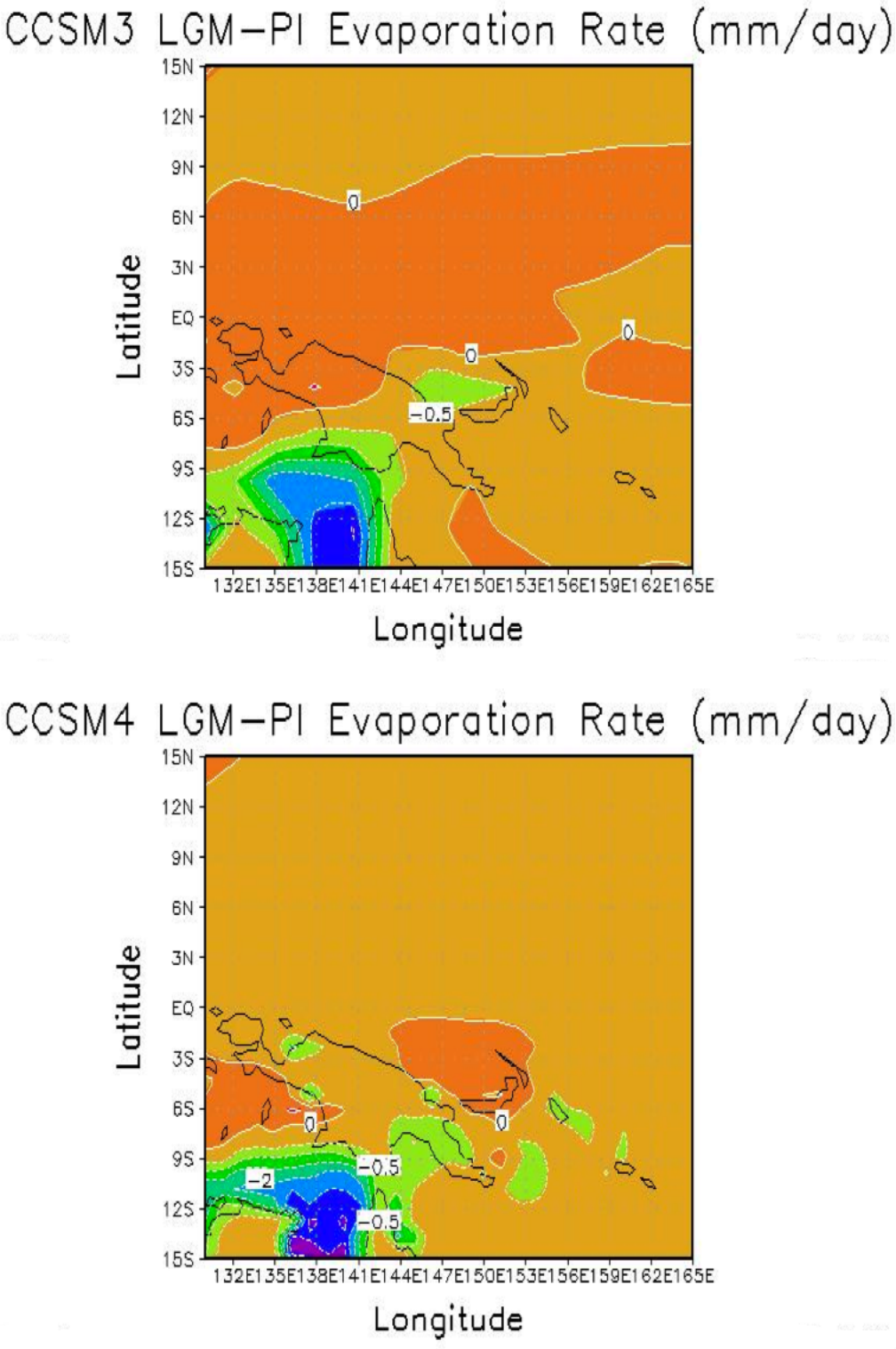

Figure 5.23: Annual mean change in evaporation rate (mm/day) for CCSM3 (top) and CCSM4 (bottom) calculated as LGM-PI runs and contoured at -3, -2.5, -2, -1.5, -1, -0.5, 0, and 0.5 mm/day.

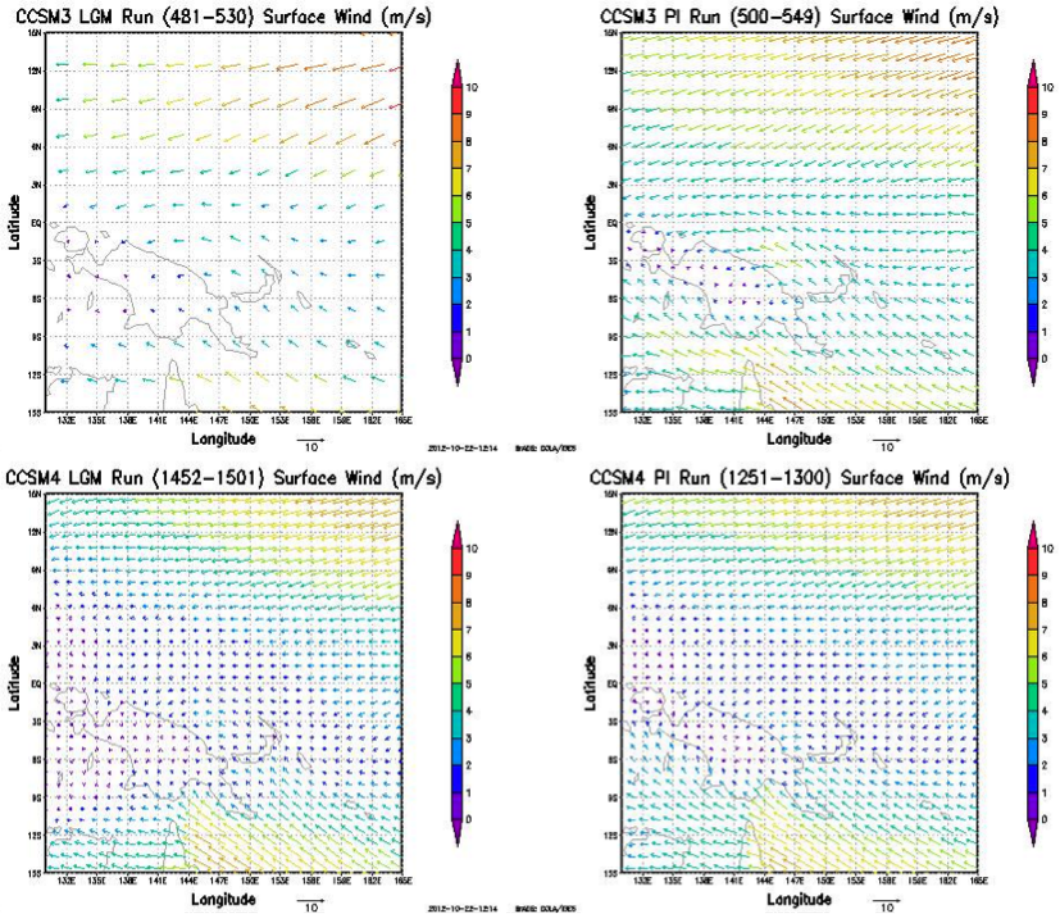

Figure 5.24: Annual mean surface wind vectors for CCSM3 (top) and CCSM4 (bottom). The length of the vector is proportional to wind speed (m/s).

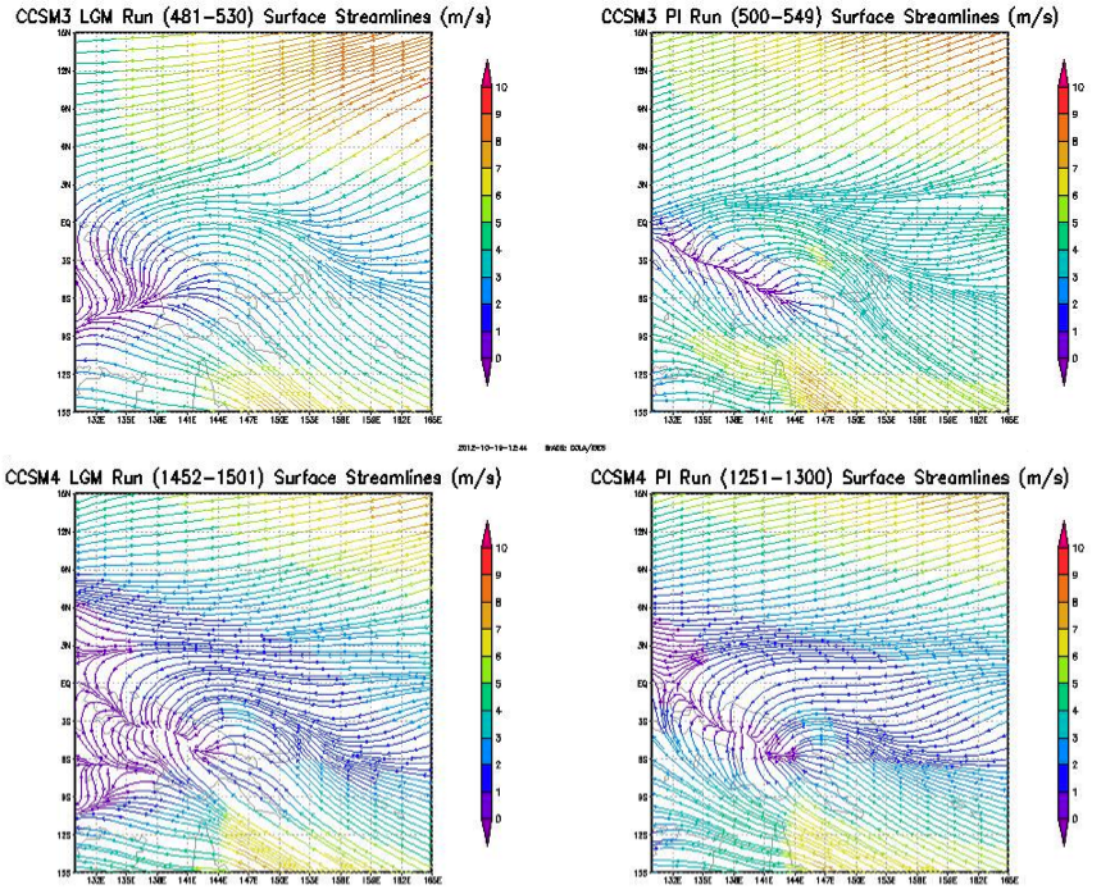

Figure 5.25: WPWP surface streamlines representing the transport of air and moisture in and around the warm pool. Streamlines are colored according to speed in m/s.

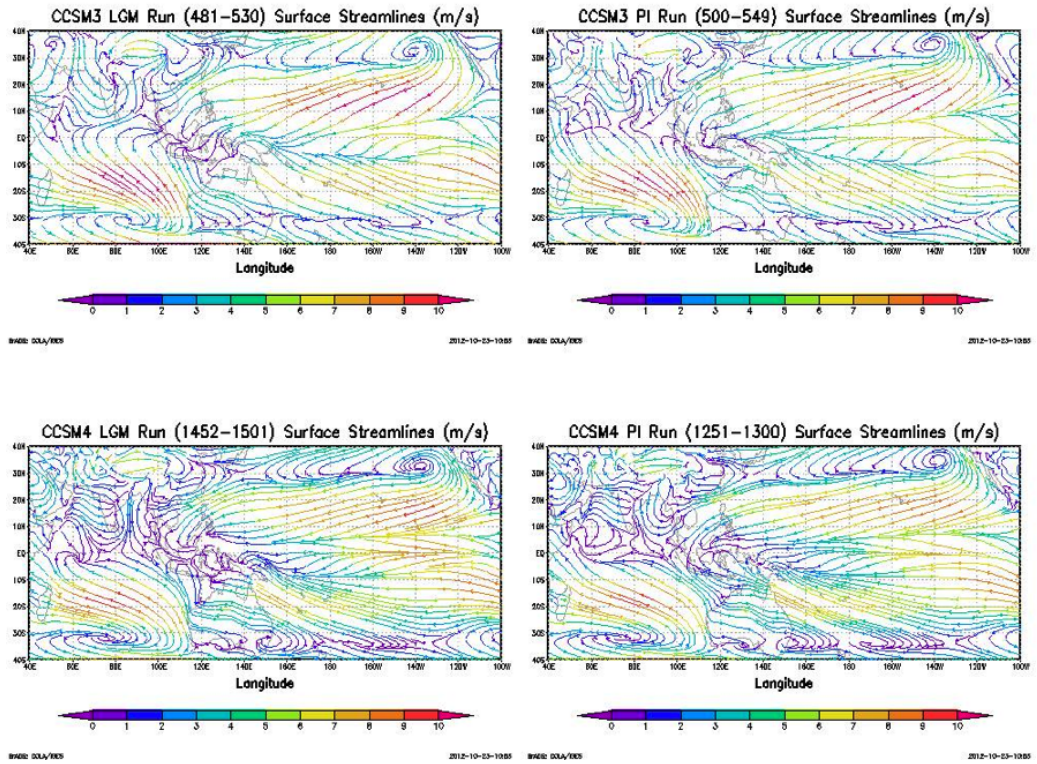

Figure 5.26: Extended region into the Pacific and Indian Oceans of surface streamlines (m/s) representing surface air and moisture transport into the WPWP for CCSM3 (top) and CCSM4 (bottom).

References

[1] Adkins, J.F., K. McIntyre and D.P. Schrag (2002), The salinity, temperature, and 18O of the glacial deep ocean, *Science*, 298(5599), 1769-1773, doi: 10.1126/science.1076252

[2] Barrows, T.T., G.S. Hope, M.L. Prentice, L.K. Fifield and S.G. Tims (2011), Late Pleistocene glaciation of the Mt. Giluwe volcano, Papua New Guinea, *Quaternary Science Reviews*, 30(19-20), 2676-2689, doi: 10.1016/j.quascirev.2011.05.022

[3] Beck, J.W., R.L. Edwards, E. Ito, F.W. Taylor, J. Recy, F. Rougerie, P. Joannot and C. Henin (1992), Sea-surface temperature from coral skeletal strontium calcium ratios, *Science*, 257(5070), 644-647, doi: 10.1126/science.257.5070.644

[4] Bitz, C.M., K.M. Shell, P.R. Gent, D.A. Bailey, G. Danabasoglu, K.C. Armour, M.M Holland and J.T. Kiehl (2012), Climate sensitivity of the community climate system model, version 4, *Journal of Climate*, 25(9), 3053-3070, doi: 10.1175/JCLI-D-11-00290.1

[5] Braconnot, P., B.L. Otto-Bliesner, S. Harrison, S. Joussaume, J.Y. Peterchmitt, A. Abe-Ouchi, M. Crucifix, E. Driesschaert, T. Fichefet, C.D. Hewitt, M. Kageyama, A. Kitoh, A. Laine, M.F. Loutre, O. Marti, U. Merkel, G. Ramstein, P. Valdes, S.L. Weber, Y. Yu, and Y. Zhao (2007), Results of PMIP2 coupled simulations of the mid-Holocene and last glacial maximum part 1: Experiments and large-scale features, *Climate of the Past*, 3(2), 261-277

[6] Broccoli, A.J. and S. Manabe (1987), The influence of continental ice, atmospheric CO2, and land albedo on the climate of the last glacial maximum, *Climate Dynamics*, 1(2), 87-99, doi: 10.1007/BF01054478

[7] Brown, R.G. and C.D. Zhang (1997), Variability of midtropospheric moisture and its effect on cloud-top height distribution during TOGA COARE, *Journal of the Atmospheric Sciences.*, 54(23), 2760-2774

[8] CLIMAP Project Members (1976), The surface of the ice-age earth: Quantitative geologic evidence is used to reconstruct boundary conditions for the climate 18,000 years ago, *Science*, 191, 1131-1137, doi: 10.1126/science.191.4232.1131

[9] CLIMAP Project Members (1984), The last interglacial ocean, *Quaternary Research*, 21, 123-224

[10] Collins, W.D., P.J. Rasch, B.A. Boville, J.J. Hack, J.R. McCaa, D.L. Williamson, J.T. Kiehl, B. Briegleb, C. Bitz, S. Lin, M. Zhang and Y. Dai (2004), Description of the NCAR Community Atmosphere Model (CAM 3.0), NCAR Technical Note

[11] Collins, W.D., C.M. Bitz, M.L. Blackmon, G.B. Bonan, C.S. Bretherton, J.A. Carton, P. Chang, S.C. Doney, J.J. Hack, T.B. Henderson, J.T. Kiehl, W.G. Large, D.S. McKenna, B.D. Santer and R.D. Smith (2006), The Community Climate System Model version 3 (CCSM3), *Journal of Climate*, 19(11), 2122-2143, doi: 10.1175/JCLI3761.1

[12] Dallenbach, A., T. Blunier, J. Fluckiger, B. Stauffer, J. Chappellaz and D. Raynaud (2000), Changes in the atmospheric CH4 gradient between Greenland and Antarctica during the last glacial and the transition to the Holocene, *Geophysical Research Letters*, 27(7), 1005-1008, doi: 10.1029/1999GL010873

[13] de Garidel-Thoron, T., Y. Rosenthal, L. Beaufort, E. Bard, C. Sonzogni and A.C. Mix (2007), A multiproxy assessment of the western equatorial Pacific hydrography during the last 30 kyr, *Paleoceanography*, 22(3), PA3204, doi: 10.1029/2006PA001269

[14] DiNezio, P.N., A. Clement, G.A. Vecchi, B. Soden, A.J. Broccoli, B.L. Otto-Bliesner, and P. Braconnot (2011), The response of the Walker circulation to last glacial maximum forcing: Implications for detection in proxies, *Paleoceanography*, 26, PA3217, doi: 10.1029/2010PA002083

[15] Eagle, R.A., E.A. Schauble, A.K. Tripati, T. Tutken, R.C. Hulbert and J.M. Eiler (2010), Body temperatures of modern and extinct vertebrates 13C-18O bond abundances in bioapatite, *PNAS*, 107(23), 10377-10382, doi: 10.1073/pnas.0911115107

[16] Eiler, J.M. (2007), "Clumped-isotope" geochemistry-The study of naturally-occurring multiply substituted isotopologues. *Earth and Planetary Science Letters*, 262(3-4), 309-327, doi: 10.1016/j.epsl.2007.08.020

[17] Fluckiger, J., A. Dallenbach, T. Blunier, B. Stauffer, T.F. Stocker, D. Raynaud and J.M. Barnola (1999), Variations in atmospheric N2O concentration during abrupt climatic changes, *Science*, 285(5425), 227-230, doi: 10.1126/science.285.5425.227

[18] Gent, P.R., G. Danabasoglu, L.J. Donner, M.M. Holland, E.C. Hunke, S.R. Jayne, D.M. Lawrence, R.B. Neale, P.J. Rasch, M. Vertenstein,

P.H. Worley, Z.L. Yang and M.H. Zhang (2011), The community climate system model version 4, *Journal of Climate*, 24(19), 4973-4991, doi: 10.1175/2011JCLI4083.1

[19] Ghosh, P., J. Adkins, H. Affek, B. Balta, W.F. Guo, E.A. Schauble, D. Schrag and J.M. Eiler (2006), 13C-18O bonds in carbonate minerals: A new kind of paleothermometer, *Geochimica et Cosmochimica Acta*, 70(6), 1439-1456, doi: 10.1016/j.gca.2005.11.014

[20] Guilderson, T.P., G. Richard, G. Fairbanks and J.L. Rubenstone (1994), Tropical temperature variations since 20,000 years ago: Modulating interhemispheric climate change, *Science*, 263(5147), 663-665, doi: 10.1126/science.263.5147.663

[21] Harrison, S.P., P. Braconnot, S. Joussaume, C. Hewitt and R.J. Stouffer (2002), Fourth international workshop of The Palaeoclimate Modelling Intercomparison Project (PMIP): launching PMIP Phase II, EOS

[22] Hastenrath, S. (2009), Past glaciation in the tropics, *Quaternary Science Reviews*, 28(9-10), 790-798, doi: 10.1016/j.quascirev.2008.12.004

[23] Holloway, C.E. and J.D. Neelin (2009), Moisture vertical structure, column water vapor, and tropical deep convection, *Journal of the Atmospheric Sciences*, 66(6), 1665-1683, doi: 10.1175/2008JAS2806.1

[24] Hostetler, S.W. and P.U. Clark (2000), Tropical climate at the last glacial maximum inferred from glacier mass-balance modeling, *Science*, 290(5497), 1747-1750, doi: 10.1126/science.290.5497.1747

[25] Hurrell, J.W., J.J. Hack, D. Shea, J.M. Caron and J. Rosinski (2008) A new sea surface temperature and sea ice boundary dataset for the Community Atmosphere Model. *Journal of Climate*, 21(19), 51455153, doi: 10.1175/2008JCLI2292.1

[26] Jensen, M.P. and A.D. Del Genio (2006), Factors limiting convective cloud-top height at the ARM Nauru Island climate research facility, *Journal of Climate*, 19(10), 2105-2117, doi: 10.1175/JCLI3722.1

[27] Joussaume, S. and K.E. Taylor (2000), The Paleoclimate Modeling Intercomparison Project, in Paleoclimate Modelling Intercomparison Project (PMIP). Proceedings of the Third PMIP workshop., edited by P. Braconnot, pp. 9-25, WCRP, La Huardiere, Canada, 4-8 October 1999

[28] Klein, A.G., G.O. Seltzer and B.L. Isacks (1999), Modern and last local glacial maximum snowlines in the central Andes of Peru, Bolivia, and northern Chile, *Quaternary Science Reviews*, 18(1), 63-84, doi: 10.1016/S0277-3791(98)00095-X

[29] Kuang, Z. and C.S. Bretherton (2006), A mass-flux scheme view of a high-resolution simulation of a transition from shallow to deep cumulus convection, *Journal of the Atmospheric Sciences*, 63(7), 1895-1909, doi: 10.1175/JAS3723.1

[30] Kucera, M., A. Rossell-Mele, R. Schneider, C. Waelbroeck and M. Weinelt (2005), Multiproxy approach for the reconstruction of the global ocean surface (MARGO), *Quaternary Science Reviews*, 24(7-9), 813-819, doi: 10.1016/j.quascirev.2004.07.017

[31] Lambeck, K., Y. Yokoyama and T. Purcell (2002), Into and out of the last glacial maximum: Sea-level change during oxygen isotope stages 3 and 2, *Quaternary Science Reviews*, 21(1-3), 343-360, doi: 10.1016/S0277-3791(01)00071-3

[32] Lea, D.W., D.K. Pak and H.J. Spero (2000), Climate impact of late quaternary equatorial Pacific sea surface temperature variations, *Science*, 289(5485), 1719-1724, doi: 10.1126/science.289.5485.1719

[33] Levis, S., J.A. Foley and D. Pollard (1999), CO2, climate, and vegetation feedbacks at the last glacial maximum, *Journal of Geophysical-Atmospheres*, 104(D24), 31191-31198, doi: 10.1029/1999JD900837

[34] MARGO Project Members (2009), Constraints on the magnitude and patterns of ocean cooling at the last glacial maximum, *Nature Geoscience*, 2(2), 127-132, doi: 10.1038/NGEO411

[35] Mathien-Blard, E. and F. Bassinot (2009), Salinity bias on the foraminifera Mg/Ca thermometry: Correction procedure and implications for past ocean hydrographic reconstructions, *Geochemistry Geophysics Geosystems*, 10(12), Q12011, doi: 10.1029/2008GC002353

[36] Meehl, G.A., W.M. Washington, J.M. Arblaster, A.X. Hu, H.Y. Teng, C. Tebaldi, B.N. Sanderson, J.F. Lamarque, A. Conley, W.G. Strand and J.B. White (2012), Climate system response to external forcings and climate change projections in CCSM4, *Journal of Climate*, 25(11), 3661-3683, doi: 10.1175/JCLI-D-11-00240.1

[37] Monnin, E., A. Indermuhle, A. Dallenbach, J. Fluckiger, B. Stauffer, T.F. Stocker, D. Raynaud and J.M. Barnola (2001), Atmospheric CO2 concentrations over the last glacial termination, *Science*, 291(5501), 112-114, doi: 10.1126/science.291.5501.112

[38] Neale, R.B., J.H. Richter and M. Jochum (2008), The impact of convection on ENSO: From a delayed oscillator to a series of events, *Journal of Climate*, 21(22), 5904-5924, doi: 10.1175/2008JCLI2244.1

[39] Neale, R.B., J.H. Richter, A.J. Conley, S. Park, P.H. Lauritzen, A. Gettelman, D. Williamson, P.J. Rasch, S.J. Vavrus, M.A. Taylor, W.D. Collins, M. Zhang and S.J. Lin (2010), Description of the NCAR Community Atmosphere Model (CAM 4.0), NCAR Technical Note

[40] O'Gorman, P.A. and C.J. Muller (2010), How closely do changes in surface and column water vapor follow Clausius-Clapeyron scaling in climate change simulations?, *Environmental Research Letters*, 5, doi:10.1088/1748-9326/5/2/025207

[41] Pausata, F.S.R., C. Li, J.J. Wettstein, M. Kageyama and K.H. Nisancioglu (2011), The key role of topography in altering North Atlantic atmospheric circulation during the last glacial period, *Climate of the Past*, 7(4), 1089-1101, doi: 10.5194/cp-7-1089-20111

[42] Peltier, W.R. (1994), Ice-age paleotopography, *Science*, 265(5169), 195-201, doi: 10.1126/science.265.5169.195

[43] Peltier, W.R. (1996), Mantle viscosity and ice-age ice sheet topography, *Science*, 273(5280), 1359-1364, doi: 10.1126/science.273.5280.1359

[44] Peltier, W.R. (2002), Global glacial isostatic adjustment: paleogeodetic and space-geodetic tests of the ICE-4G (VM2) model, *Journal of Quaternary Science*, 17(5-6), 491-510, doi: 10.1002/jqs.713

[45] Peltier. W.R. (2004), Global glacial isostasy and the surface of the ice-age earth: The ICE-5G (VM2) model and GRACE, *Annual Review of Earth and Planetary Science*, 32, 111-149, doi: 10.1145/annurev.earth.32.082503.144359

[46] Peterschmitt, J.Y. (2010), Ice sheet for PMIP3/CMIP5 simulations, PMIP3, March 3, 2010 <https://wiki.lsce.ipsl.fr/pmip3/doku.php/pmip3:design:pi:final:icesheet>

[47] Pierrehumbert, R.T. (1999), Huascaran delta 18O as an indicator of tropical climate during the last glacial maximum, *Geophysical Research Letters*, 26(9), 1345-1348, doi: 10.1029/1999GL900183

[48] Pierrehumbert, R.T. (2000), Climate change and the tropical Pacific: The sleeping dragon wakes, Proceedings of the National Academy of Sciences, 97(4), 1355-1358, doi: 10.1073/pnas.97.4.1355

[49] Porter, S.C. (2001), Snowline depression in the tropics during the last glaciation, *Quaternary Science Reviews*, 20(10), 1067-1091

[50] Prentice, M.L., G.S. Hope, K. Maryunani and J.A. Peterson (2005), An evaluation of snowline data across New Guinea during the last major glaciation and area-based glacier snowlines in the Mt. Jaya region of Papua, Indonesia, during the LGM, *Quaternary Science Reviews*, 138-139, 93-117, doi: 10.1016/j.quaint.2005.02.008

[51] Prentice, M.L. and S. Glidden (2010), Glacier crippling and the rise of the snowline in western New Guinea (Papua Province, Indonesia) from 1972 to 2000, Altered Ecologies: Fire, *Climate and Human Influence on Terrestrial Landscapes*, 32, 457-471

[52] Raymond, D.J. and A.M. Blyth (1986), A stochastic mixing model for nonprecipitating cumulus clouds, *Journal of the Atmospheric Sciences*, 43, 2708-2718

[53] Raymond, D.J. and A.M. Blyth (1992), Extension of the stochastic mixing model to cumulonimbus clouds, *Journal of the Atmospheric Sciences*, 49(21), 1968-1983, doi: 10.1175/1520-0469(1992)049¡1968:EOTSMM¿2.0.CO;2

[54] Richter, J.H. and P.J. Rasch (2008), Effects of convective momentum transport on the atmospheric circulation in the community atmosphere model, version 3, *Journal of Climate*, 21(7), 1487-1499, doi: 10.1175/2007JCLI1789.1

[55] Rosenthal, Y., M. P. Field, and R. M. Sherrell (1999), Precise determination of element/calcium ratios in calcareous samples using sector field inductively coupled plasma mass spectrometry, *Analytical Chemistry*, 71(15), 32483253, doi: 10.1021/ac981410x

[56] Sahany, S., J.D. Neelin, K. Hales and R.B. Neale (2012), Temperature-moisture dependence of the deep convective transition as a constraint on entrainment in climate models, *Journal of the Atmospheric Sciences*, 69(4), 1340-1358, doi: 10.1175/JAS-D-11-0164.1

[57] Schauble, E.A., P. Ghosh and J.M. Eiler (2006), Preferential formation of 13C-18O bonds in carbonate minerals, estimated using first-principles lattice dynamics, *Geochimica et Cosmochimica Acta*, 70(10), 2510-2529, doi: 10.1016/j.gca.2006.02.011

[58] Sobel, A.H., S.E. Yuter, C.S. Bretherton and G.N. Kiladis (2004), Large-scale meteorology and deep convection during TRMM KWAJEX, *Monthly Weather Review*, 132(2), 422-444, doi: 10.1175/1520-0493(2004)132¡0422:LMADCD¿2.0.CO;2

[59] Song, X. and G.J. Zhang (2009), Convection parameterization, tropical Pacific double ITCZ, and upper-ocean biases in the NCAR CCSM3. Part 1: Climatology and atmospheric feedback, *Journal of Climate*, 22(16), 4299-4315, doi: 10.1175/2009JCLI2642.1

[60] Tripati, A.K., R.A. Eagle, N. Thiagarajan, A.C. Gagnon, H. Bauch, P.R. Halloran and J.M. Eiler (2010), 13C-18O isotope signatures and clumped isotope' thermometry in foraminifera and coccoliths, *Geochimica et Cosmochimica Acta*, 74(20), 5697-5717, doi: 10.1016/j.gca.2010.07.006

[61] Tripati, A.K., S. Sahany, D. Pittman, R.A. Eagle, J.D. Neelin, J.M. Eiler, J.L. Mitchell, and L. Beaufort (2012), Clumped isotope temperatures and entrainment explain glacial to recent tropospheric structure over the west Pacific warm pool, In review to *Nature*

[62] Vertenstein, M., T. Craig, T. Henderson, S. Murphy, G.R. Jr. Carr, and N. Norton, CCSM3.0 User's Guide, National Center for Atmospheric Research, Boulder, CO, 25 Jun 2004

[63] Yin, J. and D. Battisti (2001), The importance of tropical sea surface temperature patterns in simulations of last glacial maximum climate, *Journal of Climate*, 14(4), 565-581, doi: 10.1175/1520-0442

[64] Zhang G.J. and N.A. McFarlane (1995), Sensitivity of climate simulations to the parameterization of cumulus convection in the Canadian Center general-circulation model, *Atmosphere-Ocean*, 33(3), 407-446